FINITE ELEMENT MODEL FOR INTERFACES IN COMPATIBILIZED POLYMER BLENDS.

S.N.R. Mudunuru

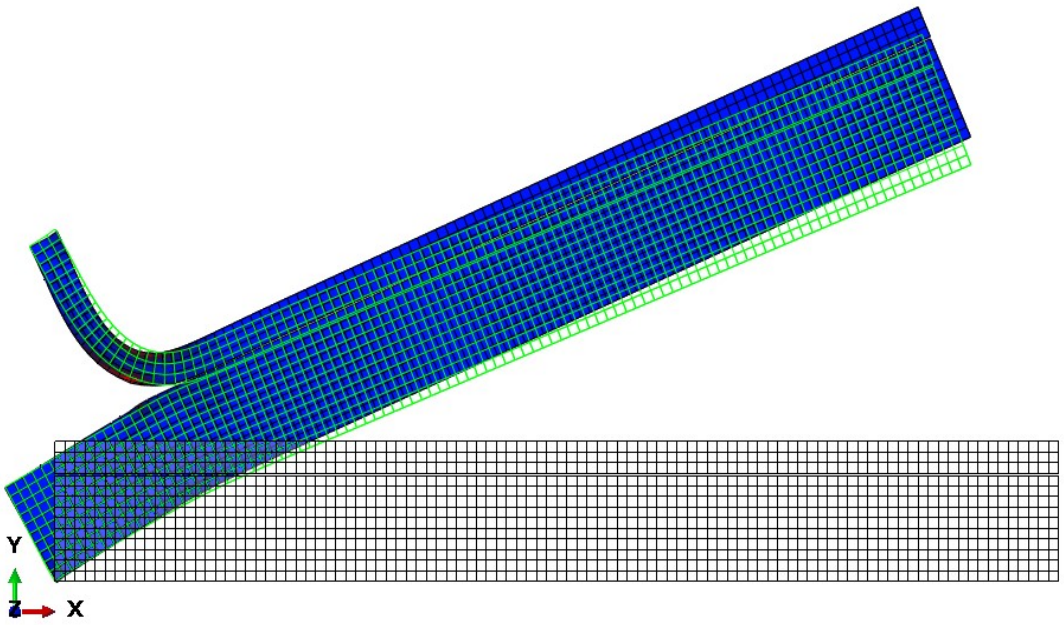

TU Delft

Master Thesis

Finite Element Model For Interfaces In Compatibilized Polymer Blends.

A Comparative Study on the Mixed-Mode Response of Cohesive Zone Models Implemented With Small and Large Displacement Assumptions.

by

Satya Nanditha Raj Mudunuru

submitted to Delft University of Technology
in partial fulfillment of the requirements for the degree of
Master of Science in Materials Science and Engineering.

Student number:	5035465
Project duration:	April 1, 2021 – March 30, 2022
Graduation Committee:	Dr. Miguel A. Bessa, TU Delft
	Dr. A. Turon Travesa, Universitat de Girona
	Dr. Boyang Chen, TU Delft

ISBN 978-94-6366-528-5
An electronic version of this thesis is available at
http://repository.tudelft.nl/.

TU Delft

Acknowledgments

I would like to thank Miguel for allowing me to work with him and the team on this project, for his input, and for constantly encouraging me to do and be better. I am forever indebted to him for everything I have learned during this period. I would also like to thank Albert for his invaluable input, critical comments, and guidance at every step. Further, I would like to extend my gratitude to the graduation committee for reviewing my work. Finally, I would like to thank my family and friends for their encouragement and support. None of this would have been possible without you.

Summary

Designing and modeling compatibilized polymer blends require accurate interface model. In addition, it is possible that crazing occurs during failure of the interfaces leading to large deformation prior to complete failure and therefore must be accounted for by the interface model.

A preliminary literature review showed that existing formulations for the large deformation account for the nonlinearity by adjusting the assumptions. For example, Van den Bosch et al. (2007) proposed redefining the local basis at each integration point. In contrast, Reinoso and Paggi (2014) argued that this did not account for geometric nonlinearity and proposed including the first derivative of rotation vector in the finite element equation. However, the mixed-mode responses of the models were not characterized and validated thoroughly. Therefore, we studied the response from standardized mixed-mode tests to compare the large displacement formulation with the commonly used small-displacement formulation of the cohesive zone model.

The standardized tests used by Moreira et al. (2020) for characterizing the mixed-mode behavior of ductile interfaces inspired the tests used in this study. When implemented with the BK criteria, the mode partitioning method used by Moreira et al. (2020) results in a wider spread of the mean predicted mode ratio and the mean predicted fracture toughness. However, the corresponding mode ratio predictions are similar when the predicted fracture toughness is close to expected. Therefore, while the power-law is better for implementing the mode partitioning method, we can use the predictions from the mode partitioning method implemented with the power-law to find the BK parameter.

Further, simulating the mixed-mode fracture tests with properties presented by Moreira et al. (2020) showed that bulk materials with high modulus or stiffness, such as carbon fiber reinforced plastics, do not undergo nonlinear deformation to require the large deformation formulation. However, for bulk materials with lower modulus or stiffness, the responses of the two formulations in question are different. Additionally, for a given load case, a cohesive zone with anisotropic fracture properties experiences a different mode ratio when implemented with the large displacement formulation than the small displacement formulation. Moreover, more significant influence of the stronger mode on the load case results in greater difference between the mode ratio experienced at the interface. Nevertheless, the large displacement formulation is also applicable for stronger mode-II interfaces. However, a further investigation involving physical experiments is required to compare the response of the two formulations to the behavior of real material systems.

Contents

List of Tables

List of Figures

Nomenclature

List of Abbreviations

ADCB asymmetric double cantilever beam

ASLB asymmetric single-leg bending

CFRP carbon fiber reinforced plastics

CZM cohesive zone model

DCB double cantilever beam

DOE design of experiments

ENF end notch flexure

FE finite element

FEM finite element method

iPP isotactic polypropylene

LDF large displacement formulation

LEFM linear elastic fracture mechanics

ML machine learning

MMB mixed-mode bending

MPM mode partitioning method

PE polyethylene

PP polypropylene

SEM scanning electron microscopy

SDF small displacement formulation

SLB single-leg bending

TEM transmission electron microscopy

TSL traction separation law

Variable Notation

X, x	Scalars
$\mathbf{X}$	Vectors and tensors in the original configuration.
$\mathbf{x}$	Vectors and tensors in the current configuration.

Symbols

	Symbol	Operation
Euclidean distance	$\|\circ\|$	$\sqrt{\sum_{i=1}^{n} \circ_i^2}$
MacAuley operator	$\left\langle \circ \right\rangle$	$\frac{1}{2}(\circ + \|\circ\|)$
Dot product	$\langle \mathbf{a}, \mathbf{b} \rangle$	$\sum_{i=1}^{n} a_i b^i$
Vector projection	$Proj_{\mathbf{u}}(\mathbf{v})$	$\frac{\langle \mathbf{u},\mathbf{v} \rangle}{\langle \mathbf{u},\mathbf{u} \rangle}\mathbf{u}$

1 Introduction

Plastic waste is a severe ecological and economic issue. According to Geyer et al. (2017), as of 2015, the plastic industry manufactured approximately 8.3 billion metric tons of material since conception, and 6.3 billion metric tons of that total has reached the end of life and is now plastic waste. However, only 9% of the waste was recycled and 12% incinerated, while the rest ended up in landfills or the natural environment. Geyer et al. (2017) presented the following estimates for the year 2050 based on historical trends in plastic production, consumption, and life cycles:

> *The cumulative plastic waste will amount to roughly 25 billion metric tons, and close to 50% of the total will end up in landfills or the natural environment.*

These projections by Geyer et al. (2017) account for different plastics, including thermoplastics, thermosets, polyurethanes, elastomers, coatings, and sealants. While most of them usually end up in the same waste stream, it is crucial to separate them, as most commonly used polymers are not compatible with each other. A small amount of a different polymer contaminates the material and degrades its properties due to this incompatibility (Dorigato, 2021, p. 55).

Dorigato (2021) reviewed the potential of polymer blends recycling. Their review showed that the tailored performance of the mixtures is highly flexible and depends on blend formulation and the recycling and reprocessing steps. Therefore, modeling these effects will help tailor the blends' mechanical response.

First, section 1.1 presents some techniques for modeling and designing such composite materials. Then, section 1.2 examines the work of Eagan et al. (2017), who synthesized block copolymers of different chemical compositions as compatibilizers for PE and iPP blends and studied the influence of these compatibilizers on the mechanical behavior of the blends.

The study discussed in section 1.2 showed that the compatibilizer's composition affects the blends' mechanical response. Therefore, the microstructure model must include the interaction between the bulk phases. Section 1.3 reviews some models that can account for the behavior of these interfaces. Then, section 1.4 establishes the knowledge gaps and, subsequently, the goals of this literature review.

1.1 Design and Modeling of Composites

Over the past two decades, multiscale modeling has gained much traction in simulating composite materials. Many studies implemented this procedure to simulate different types of mechanical behavior, including elastic behavior (García-Macías et al., 2019), compression (Li and Chou, 2006), viscoelastic behavior (Liu et al., 2018), fracture (Gonzalez and Llorca, 2006), and failure (Xia et al., 2001), to name a few, as well as different scales of interest. While Liu et al. (2018), Gonzalez and Llorca (2006), and Xia et al. (2001) focused on mapping micromechanical behavior to mesoscale behavior, García-Macías et al. (2019) and Li and Chou (2006) mapped the atomistic model to micromechanical behavior.

This strategy entails defining the system at different scales of interest and obtaining effective solutions at each of these scales. Then, one can homogenize the solutions over the corresponding length scale to transfer the effects up the scale ladder. This method allows us to virtually test complex structures and materials. Llorca et al. (2013) presented a road map to use multiscale modeling for virtual testing and process optimization for fiber-reinforced materials.

Bessa et al. (2017) proposed a data-driven framework for using machine learning to design and model material systems. They demonstrated the potential of this computational framework by finding the general constitutive model for a 2D hyper-elastic composite. They also used the framework to design a 3D inelastic composite.

One can implement this framework by defining the following components for the mechanics of the material:

- Representative model for the microstructure.
- Material constitutive models and parameters for the phases in the microstructure.
- Loading conditions.

Based on the design objectives, relevant parameters are optimized using the framework, which starts by exploring the design space with the appropriate design of experiments (DOE). Next, at each point in the DOE, the computational models are implemented to generate a database. Finally, machine learning (ML) algorithms capture the relationship between the input parameters and the objective.

An essential first step to implementing either of these techniques for designing or modeling composite materials and structures is defining and validating constitutive models of the individual phases in the composite and a representative microstructure model. Therefore, section 1.2 surveys the mechanical behavior of compatibilized blends for the case of PE - iPP mixtures presented by Eagan et al. (2017) to better understand the requirements for modeling the microstructure.

1.2 Compatibilized Polymer Blends

Eagan et al. (2017) synthesized PE-iPP block copolymers as compatibilizers for PE and iPP blends. The block copolymers have segments of both homopolymers. Therefore, thermodynamically, these segments favor being surrounded by their corresponding bulk

phases. Given enough mobility, the copolymer segments tend to embed themselves into the corresponding bulk phases, thereby forming a network of entangled polymer chains at the interface between the bulk phases.

According to Eagan et al. (2017), this stitching process at the interface for the PE-iPP system occurs when the block copolymer is compressed between the bulk phases at processing temperature close to 180°C. Upon cooling, this stitched network at the interface binds the two homopolymer phases. The transmission electron microscopy (TEM) images (fig. 1.1 (A), fig. 1.1 (B)) of samples fabricated by compression molding the melts at said processing temperature show that the blends assume a droplet-like particle dispersion of one homopolymer phase in the other. However, the imaging does not confirm whether the transition region between the bulk phases is an interface or interphase[1]. Therefore, hereafter, we use the word *interface* as an encompassing term to refer to the transition between the bulk phases, omitting its thickness description.

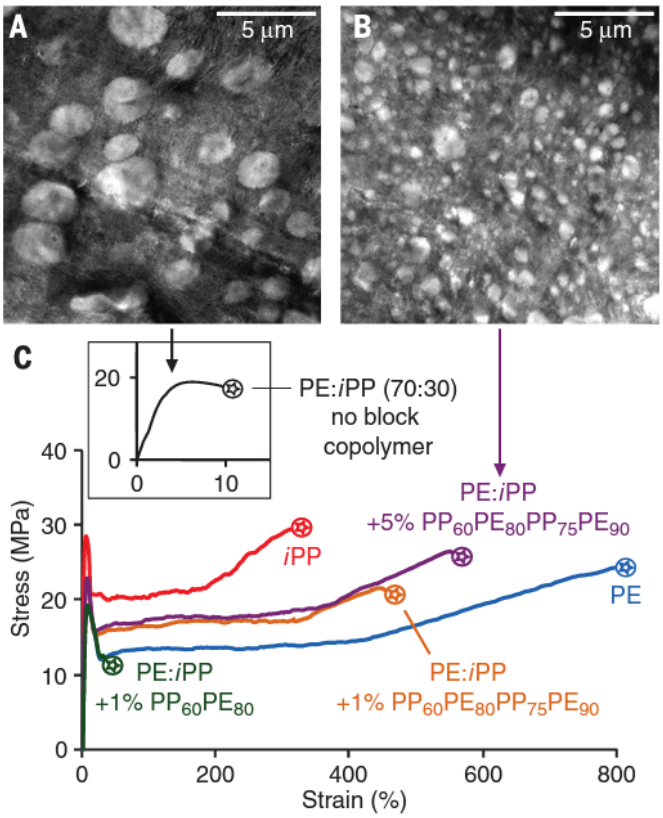

Figure 1.1: (A) TEM images of PE-iPP blend without block copolymers. (B) TEM images of PE-iPP blend with five wt% tetra block copolymers. (C) Uniaxial tensile elongation of PE/iPP materials and blends. (Eagan et al., 2017)

The influence of the block copolymers on the mechanical behavior of the blends under uniaxial tensile loading is evident from the stress-strain relationships in fig. 1.1 (C). Firstly, the addition of block copolymers considerably increases the failure strain of

[1]The term *interface* describes a surface or boundary with infinitesimal thickness relative to the length scales of the system, and the term *interphase* describes an intermediate region with a finite thickness

the blends from around 10% strain to nearly 500% for high molecular weight block copolymers. Moreover, the molecular weight, weight fraction, and composition of the block copolymers influence the response of the blends.

The block copolymers also influence the interface properties at the mesoscale. Eagan et al. (2017) conducted peel tests with specimens fabricated by compression molding rectangular plaques of PE, iPP films placed one on top of the other, with a layer of block copolymer in between them. The peel strength was determined by pulling apart the PE and iPPlayers and monitoring the response of the specimens, resulting in the strength-displacement plots in fig. 1.2. The peel test results complement the conclusions from the tensile tests. The addition of block copolymers results in stronger interfaces, and the chemical composition of the copolymers affects the nature of this improvement. Therefore, the interface properties must be accounted for when modeling the blends.

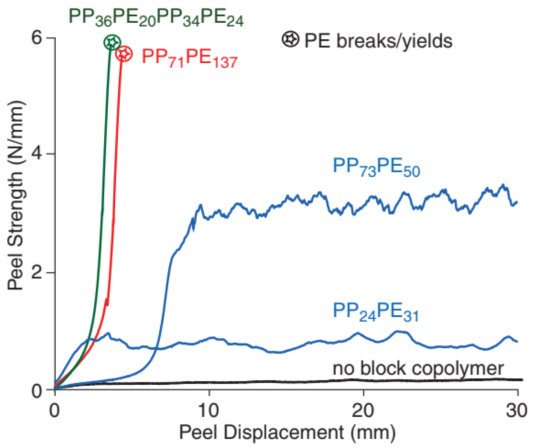

Figure 1.2: Peel strength of PE - iPP films with various block copolymer interfaces (Eagan et al., 2017).

Additionally, Eagan et al. (2017) presented scanning electron microscopy (SEM) images of the fracture surfaces of the PE, iPP films from the peel test specimens. These surfaces for specimens with (fig. 1.3) and without (fig. 1.4) a compatibilizer show that the low molecular weight compatibilizers resulted in out-of-plane polymer fibrils at the interface. This phenomenon of formation and stretching of fibrils during failure in a polymer is called crazing (Kramer and Berger, 1990).

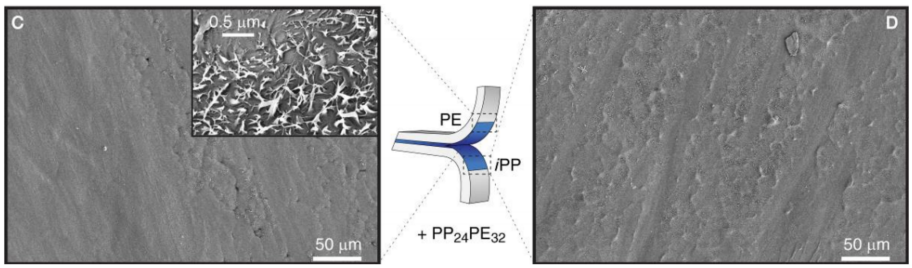

Figure 1.3: Films after peel test with low molecular weight block copolymer interfaces (Eagan et al., 2017). (C) PE film. (D) iPP film.

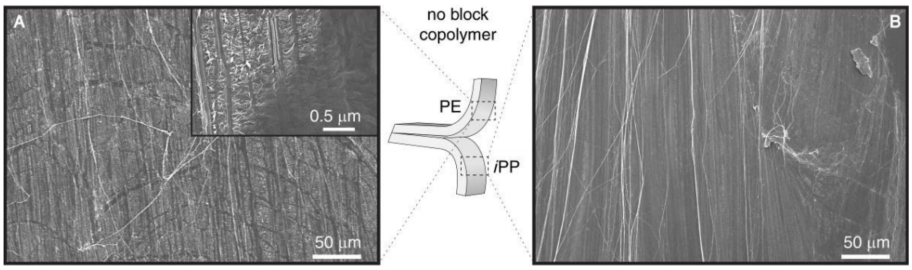

Figure 1.4: Films after peel test with no block copolymer (Eagan et al., 2017). (A) PE film. (B) iPP film.

There is no evidence that this mechanism applies to high molecular weight compatibilizers since the bulk phase materials fail before delamination occurs (Eagan et al., 2017, fig. 2). However, it is reasonable to presume that crazing would occur when the interfaces with high molecular weight block copolymers undergo cohesive failure. It is a common mechanism for cohesive failure in polymers, as evidenced by Jang et al. (1985), Kamei and Brown (1984), Lustiger and Corneliussen (1987), Argon et al. (1981), Koltisko et al. (1986), Donald and Kramer (1982), Kausch et al. (2004) Legrand (1969), Marshall et al. (1970), Lauterwasser and Kramer (1979). Therefore the interface model should be able to account for this mechanism. Therefore, section 1.3 presents a brief discussion on interface modeling for crazing.

1.3 Interface Modeling

The block copolymer chains at the interface are embedded into the bulk phases, as discussed in section 1.2. Xu et al. (1991) assumed the portion of the chain embedded in the bulk to be trapped inside a tube that prevents this chain from being pulled out. Figure 1.5 shows a schematic representation of this assumption. The force required to change the gap between the tubes taking into account the friction between the tubes and the chain gives the constitutive model of the interface.

The authors then used linear elastic fracture mechanics (LEFM) to describe the fracture toughness using stress derived from the force defined by the constitutive law and the density of block copolymer chains in the interface. However, the authors concluded that this method does not work for high crack growth rates. Further, chain pull-out is only one among the different failure mechanisms that occur during crazing and therefore does not describe the process entirely.

Instead, Tijssens et al. (2000) used cohesive surfaces to represent the crazing behavior. Cohesive surface models use the gap between the bulk phases in the constitutive law similar to the chain pull-out model. However, this method facilitates complex constitutive laws that account for relevant underlying mechanisms. Tijssens et al. (2000) proposed a three-stage law accounting for craze initiation, widening, and breakdown.

The Cohesive zone model (CZM)s, similar to the cohesive surface model used by Tijssens et al. (2000), were widely implemented for simulating interface delamination in composites. Section 2.1 presents an overview of the cohesive zone element formulation and a constitutive model. The primary feature of the cohesive zone model (CZM) and the cohesive surface model is reducing the displacements of the nodes in the damage-prone

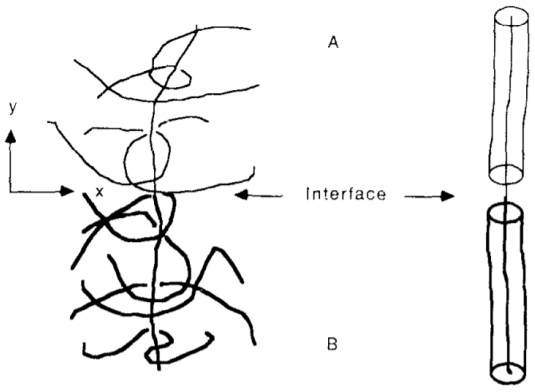

Figure 1.5: (a) Block copolymer chain embedded in the bulk phases A, B. (B) Tube representing the influence of the bulk on the copolymer chain. (Xu et al., 1991)

zones to the separation between the crack surfaces, also called displacement jump or the displacement gap or the separation. In addition, the traction separation law (TSL) gives the traction corresponding to the displacement gap.

The displacement gap and traction are incorporated into the finite element equations assuming that the elements undergo small deformation. However, modifications to the formulation are required when the elements undergo large deformation observed during crazing.

Van den Bosch et al. (2007) redefined the local element bases at each integration point to account for the orientation of the load-bearing fibrils. On the other hand, Reinoso and Paggi (2014) proposed a modification to the element kinematics to account for the geometric and material nonlinearities and ensure consistency with the assumptions of the formulation. Therefore, following Reinoso and Paggi (2014)'s reasoning, one must implement the modified formulation even when using Van den Bosch et al. (2007)'s definition of local bases.

On the other hand, from the results presented by Reinoso and Paggi (2014), their formulation seems to differ from the SDF only when the material is stronger in mode-I than mode-II (Figure 2.5a & Figure 2.5b). However, experimental studies conducted on mixed-mode characterization of ductile polymer interfaces by Wang (1997), Da Silva et al. (2011), and Costa et al. (2017) reported stronger mode-II behavior.

Nevertheless, since Reinoso and Paggi (2014) mentioned that the boundary conditions used in their mixed-mode single element tests are predominantly mode-I, one might postulate that when the load case is predominantly mode-II, the LDF will influence the mechanical response for interfaces with stronger mode-II. **Therefore, further characterization of the model concerning the mode ratio is needed.** To test this hypothesis, we present our goals for research in the following section 1.4.

1.4 Research Questions

So far, we have established that the compatibility between commonly used plastics is a concerning issue in plastic waste management. As a solution, Eagan et al. (2017) synthesized and experimentally validated the use of block copolymers as compatibilizers

for PE and iPP.

One can use state-of-the-art design frameworks discussed in section 1.1 to accelerate the design process of such composites. However, a critical step to implementing these techniques is accurately modeling the material phases in the microstructure, namely the bulk phases and the interfaces. Based on the discussion in section 1.2, the model must account for the crazing mechanism at the interface. While the model presented by Reinoso and Paggi (2014) seems promising to account for nonlinearities occurring in ductile interfaces, further characterization of mixed-mode behavior is required. That leaves us with the following questions:

> ***How do the following parameters influence the difference between the commonly used SDF and Reinoso and Paggi (2014)'s LDF?***
>
> - ***The ratio of pure mode critical energy release rates ($\frac{G_{I_C}}{G_{II_C}}$)***
> - ***Mode ratio (β)***

To address these questions, section 2.1 presents the finite element formulations suitable for modeling interfaces undergoing crazing, and section 2.2 presents standardized tests for mixed-mode characterization of ductile interfaces. Further, section 2.3 concludes chapter 2 with objectives for research. Next, chapter 3 presents the methodology to fulfill the objectives, and chapter 4 and 5 present the results from the finite element implementation of these tests. Finally, chapter 6 presents the conclusions of this study.

2 Literature Review

Implementing a CZM in a finite element (FE) framework requires defining mesh elements in the delamination zone, usually having an infinitesimal thickness or as surface elements. The separation between the nodes and a constitutive law known as TSL determines the traction imposed by these cohesive elements on the surrounding material. The TSL enforces damage initiation and evolution along the delamination zone. For example, fig. 2.1 is a schematic of CZM implementation for a double cantilever beam (DCB) model. The figure uses green springs in place of the infinitesimal thickness cohesive elements in the delamination zone to represent the constitutive relationship between traction (σ) and separation (δ) within the elements, where Γ_0 is the fracture toughness. Without going into the details, it is worth noting that many types of TSLs can be implemented with the CZM, as the figure indicates.

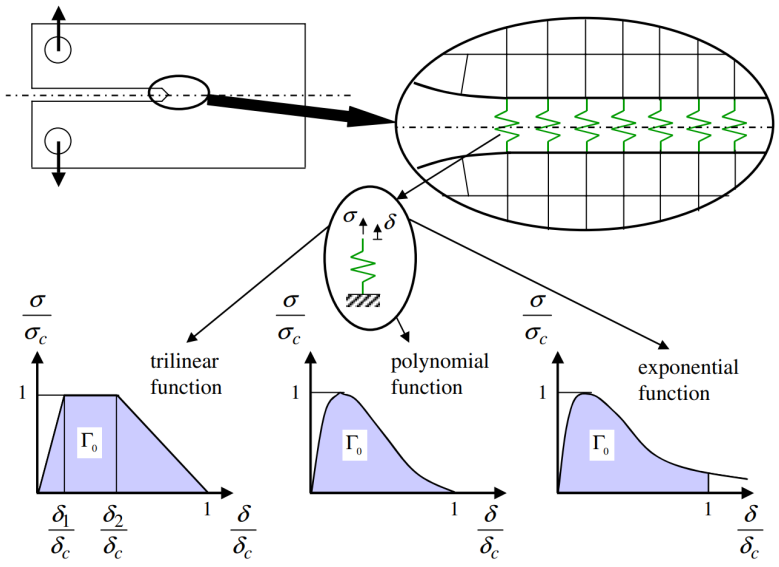

Figure 2.1: CZM with three commonly used TSLs (Pineau, 2008)

Elices et al. (2002) pointed out that CZMs are particularly useful for no initial crack problems. These models can capture both hardening and softening behavior in problems with a predefined process or failure zone. Additionally, CZMs can deal with nonlinearity

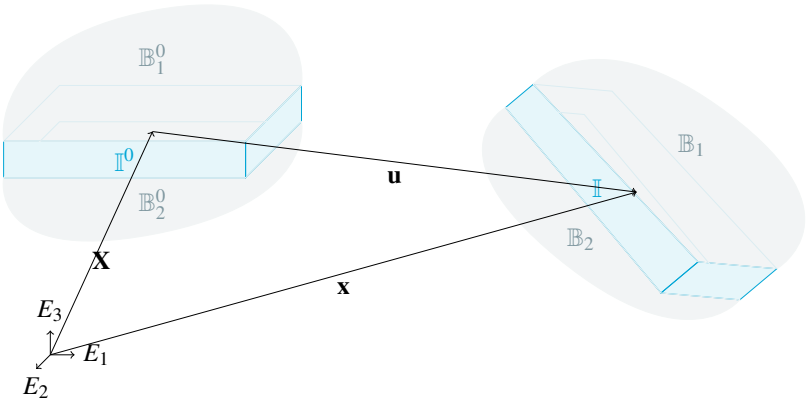

Figure 2.2: 3D Geometric definition.

ahead of the crack-tip with a good balance between accuracy and computational cost, making the CZM a good fit for our purpose of modeling the interface.

The following section describes the element kinematics for CZMs. Then, section 2.1.1 critically reviews some of the modifications proposed for large displacement similar to that observed in semi-crystalline polymers. Further, section 2.1.2 presents our choice of the TSL. We then review some standardized tests for characterizing the mixed-mode response of the formulations in section 2.2.

2.1 Finite Element Formulation

This section presents a generalization of the finite element formulation as implemented for mixed-mode infinitesimal deformation in many studies, for example, Camanho and Dávila (2002), Camanho et al. (2003), Xu and Needleman (1994), Song et al. (2006), Van den Bosch et al. (2007), Reinoso and Paggi (2014), and Jang et al. (2017).

Let us assume that a cohesive zone $\mathbb{I}$ exists between two bulk phases, $\mathbb{B}_1$ and $\mathbb{B}_2$, in an n-dimensional space $\mathbb{R}^n$ with E_n bases, as represented in fig. 2.2. The discussion here will focus on three-dimensional space. However, the 2D formulation is analogous. Let us assume that the original phases $\mathbb{I}^0$, $\mathbb{B}_1^0$, and $\mathbb{B}_2^0$ deform into $\mathbb{I}$, $\mathbb{B}_1$, and $\mathbb{B}_2$ while undergoing translation from $\mathbf{X}$ to $\mathbf{x}$. $\mathbf{X}$ and $\mathbf{x}$ represent an array of coordinates corresponding to active degrees of freedom in the reference and current configuration, respectively. Then for deformation $\mathbf{u}$ at some time $\mathbf{t}$, we can say that the following equation is true.

$$\mathbf{x} = \mathbf{X} + \mathbf{u} \tag{2.1}$$

Let us assume that the cohesive zone $\mathbb{I}$ is discretized into three-dimensional, eight-node finite elements, as represented in fig. 2.3. Nodes 1-4 represent the bottom surface of the delamination zone near phase $\mathbb{B}_2$ and nodes 5-8 represent the top near $\mathbb{B}_1$. The definition of the top and bottom sets here is arbitrary. It would be the same if we defined 1-4 as the top and 5-8 as the bottom. The only requirement here is to group all the nodes tied to a bulk phase.

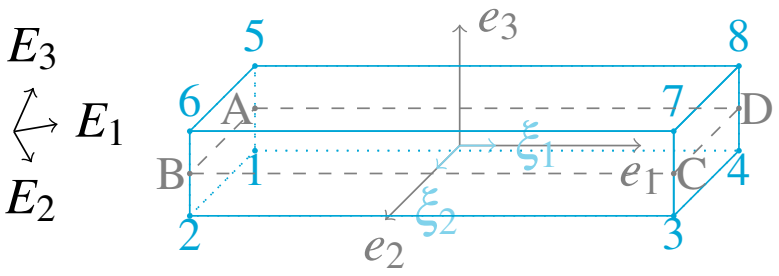

Figure 2.3: Schematic of cohesive zone element in 3D.[1]

Since only translation degrees of freedom in the directions $\mathbf{E}_1$, $\mathbf{E}_2$, $\mathbf{E}_3$ are relevant for estimating the separation vector, the vectors $\mathbf{X}$, $\mathbf{x}$, and $\mathbf{u}$ have dimensions 24×1 for the 8 node element. These element-wise vectors also conform to eq. (2.1).

Generally, one computes the mechanics of cohesive elements along the midplane of the elements, represented by the region A-B-C-D in fig. 2.3. We can determine the coordinates ($\mathbf{x_{mp}}$) of this mid-plane using the current material coordinates $\mathbf{x}$ and a matrix multiplier $\mathbf{M}$ from the following definition:

$$\begin{aligned} \mathbf{x_{mp}} &= \mathbf{M}\mathbf{x} \\ \mathbf{M} &= \frac{1}{2}\begin{bmatrix} \mathbf{I} & \mathbf{O} & \mathbf{O} & \mathbf{O} & \mathbf{I} & \mathbf{O} & \mathbf{O} & \mathbf{O} \\ \mathbf{O} & \mathbf{I} & \mathbf{O} & \mathbf{O} & \mathbf{O} & \mathbf{I} & \mathbf{O} & \mathbf{O} \\ \mathbf{O} & \mathbf{O} & \mathbf{I} & \mathbf{O} & \mathbf{O} & \mathbf{O} & \mathbf{I} & \mathbf{O} \\ \mathbf{O} & \mathbf{O} & \mathbf{O} & \mathbf{I} & \mathbf{O} & \mathbf{O} & \mathbf{O} & \mathbf{I} \end{bmatrix} \end{aligned} \tag{2.2}$$

where $\mathbf{I}$ is an identity matrix of order three and $\mathbf{O}$ is a zero matrix of the same dimensions.

In the FEM, an assumed shape function $\mathbf{N}$ approximates the continuum distribution of the nodal quantities in the element domain. Since the mid-plane is a reduced-order manifold ($\mathbb{R}^3 \to \mathbb{R}^2$), this element domain has only two natural basis vectors ξ_1, ξ_2 (fig. 2.3). One may approximate the shape function $\mathbf{N}$ using polynomials of some orders. For now, let us assume that it is linear.

Further, since our original domain is $\mathbb{R}^3$, quantities such as coordinates, deformation, and load will be three-dimensional. Therefore, we modify the shape function using $\mathbf{I}$. The following set of equations defines the shape function for the cohesive elements.

$$\begin{aligned} N_1 &= \frac{1}{4}(1-\xi_1)(1-\xi_2) \\ N_2 &= \frac{1}{4}(1+\xi_1)(1-\xi_2) \\ N_3 &= \frac{1}{4}(1+\xi_1)(1+\xi_2) \\ N_4 &= \frac{1}{4}(1-\xi_1)(1+\xi_2) \end{aligned} \tag{2.3}$$

$$\mathbf{N} = [N_i \mathbf{I}] \quad i = 1,2,3,4 \tag{2.4}$$

[1]The image has an exaggerated thickness of the element in $\mathbf{e}_3$ for demonstration purposes. Ideally, this thickness is close to zero.

We can then express the continuum approximation of the midplane as

$$\mathbf{x_m} = \mathbf{N}\mathbf{x_{mp}} = \mathbf{NMx} \tag{2.5}$$

and subsequently, determine the local bases ($\mathbf{e}_1$, $\mathbf{e}_2$, $\mathbf{e}_3$ from fig. 2.3) using its partial derivative with respect to its natural coordinates.

$$\begin{aligned} \mathbf{t}_1 &= \frac{\partial \mathbf{x_m}}{\partial \xi_1} = \frac{\partial \mathbf{N}}{\partial \xi_1}\mathbf{Mx}, \quad & \mathbf{e}_1 &= \frac{\mathbf{t}_1}{||\mathbf{t}_1||} \\ \mathbf{t}_2 &= \frac{\partial \mathbf{x_m}}{\partial \xi_2} = \frac{\partial \mathbf{N}}{\partial \xi_2}\mathbf{Mx}, \quad & \mathbf{e}_2 &= \frac{\mathbf{t}_2}{||\mathbf{t}_2||} \\ \mathbf{n} &= \mathbf{t}_1 \times \mathbf{t}_2, & \mathbf{e}_3 &= \frac{\mathbf{n}}{||\mathbf{n}||} \end{aligned} \tag{2.6}$$

Here $||\circ||$ is the euclidean norm ($\sqrt{\sum_{i=1}^{n} \circ_i^2}$). The local bases, in turn, will give us the rotation matrix $\mathbf{R}$ to transform vectors/tensors between reference coordinates ($\mathbf{E}_i$) and local coordinates ($\mathbf{e}_i$):

$$\mathbf{R} = \left[\mathbf{e}_i\right]^{-1} = \left[\mathbf{e}_i\right]^T \quad i = 1,2,3 \tag{2.7}$$

Separation Tensor:

Having defined the transformation matrices, we can now approximate the separation at the mid-plane in the element local domain. We first define a matrix multiplier $\mathbf{L}$ to determine the discretized separation ($\mathbf{G}$) in reference coordinates

$$\begin{aligned} \mathbf{G} &= \mathbf{Lu} \\ \mathbf{L} &= \begin{bmatrix} -\mathbf{I} & \mathbf{O} & \mathbf{O} & \mathbf{O} & \mathbf{I} & \mathbf{O} & \mathbf{O} & \mathbf{O} \\ \mathbf{O} & -\mathbf{I} & \mathbf{O} & \mathbf{O} & \mathbf{O} & \mathbf{I} & \mathbf{O} & \mathbf{O} \\ \mathbf{O} & \mathbf{O} & -\mathbf{I} & \mathbf{O} & \mathbf{O} & \mathbf{O} & \mathbf{I} & \mathbf{O} \\ \mathbf{O} & \mathbf{O} & \mathbf{O} & -\mathbf{I} & \mathbf{O} & \mathbf{O} & \mathbf{O} & \mathbf{I} \end{bmatrix} \end{aligned} \tag{2.8}$$

where $\mathbf{I}$, $\mathbf{O}$ have the same description as above.

We then use the shape function to approximate the distribution of separation over the continuum in the reference coordinates

$$\mathbf{G} = \mathbf{NLu} \tag{2.9}$$

and the rotation matrix to transform it to the element local coordinates.

$$\mathbf{g} = \mathbf{RNLu} \tag{2.10}$$

The local separation ($\mathbf{g}$) induces local traction (τ) based on the TSL and vice versa. Section 2.1.2 will discuss the details of this relationship. Let us now focus on the contribution of the cohesive zone to the finite element equation.

Finite Element Equation:

For local traction τ and separation $\mathbf{g}$, we can express the virtual variation in each element using the following eq. (2.11).

$$\begin{aligned}\delta\Pi_{\mathbb{I}} &= \int_{\mathbb{I}} \left(\frac{\partial \mathbf{g}}{\partial \mathbf{u}}\delta\mathbf{u}\right)^T \tau d\mathbb{I} \\ &= \delta\mathbf{u}^T \int_{\mathbb{I}} \left(\frac{\partial \mathbf{g}}{\partial \mathbf{u}}\right)^T \tau d\mathbb{I}\end{aligned} \tag{2.11}$$

Equation (2.11) is also valid at the element level. For region $\mathbb{I}^e$ of the element, Equation (2.11) becomes

$$\delta\Pi_{\mathbb{I}^e} = \delta\mathbf{u}^T \int_{\mathbb{I}^e} \left(\frac{\partial \mathbf{g}}{\partial \mathbf{u}}\right)^T \tau d\mathbb{I}^e \tag{2.12}$$

The deformed area $d\mathbb{I}$ can be expressed in the natural coordinates $d\mathbb{I}_{\xi_1,\xi_2}$ using the expression $d\mathbb{I} = ||e_1 \times e_2|| d\mathbb{I}_{\xi_1,\xi_2} = J d\mathbb{I}_{\xi_1,\xi_2}$. Therefore, the virtual variation can be rewritten as

$$\delta\Pi_{\mathbb{I}^e} = \delta\mathbf{u}^T \int_{\xi_1,\xi_2} \left(\frac{\partial \mathbf{g}}{\partial \mathbf{u}}\right)^T \tau J d\mathbb{I}^e_{\xi_1,\xi_2} \tag{2.13}$$

From the variational equation $\delta\Pi_{\mathbb{I}^e} = \delta\mathbf{u}^T\mathbf{f}^e$ where $\mathbf{f}^e$ is the internal load and the standard linearization in the FEM $\mathbf{K}^e = \partial\mathbf{f}^e/\partial\mathbf{u}$ where $\mathbf{K}^e$ is the element stiffness matrix; we can express the residual vector $\mathbf{f}$ and stiffness matrix $\mathbf{K}^e$ using the following equations:

$$\begin{aligned}\mathbf{f}^e &= \int_{\xi_1,\xi_2} \left(\frac{\partial \mathbf{g}}{\partial \mathbf{u}}\right)^T \tau J d\mathbb{I}^e_{\xi_1,\xi_2} \\ \mathbf{K}^e &\approx \int_{\xi_1,\xi_2} \left(\frac{\partial \mathbf{g}}{\partial \mathbf{u}}\right)^T \frac{\partial \tau}{\partial \mathbf{u}} J d\mathbb{I}^e_{\xi_1,\xi_2} \\ &= \int_{\xi_1,\xi_2} \left(\frac{\partial \mathbf{g}}{\partial \mathbf{u}}\right)^T \frac{\partial \tau}{\partial \mathbf{g}} \left(\frac{\partial \mathbf{g}}{\partial \mathbf{u}}\right) J d\mathbb{I}^e_{\xi_1,\xi_2}\end{aligned} \tag{2.14}$$

Here, $\frac{\partial \tau}{\partial \mathbf{g}}$ is the constitutive element stiffness matrix determined from the TSL. Additionally, note that we have ignored the geometric contribution $\left(\frac{\partial^2 \mathbf{g}}{\partial \mathbf{u}^2}\tau\right)$ to the stiffness matrix. The assumption here is that deformation before failure in the elements is small enough (infinitesimal) that the term $\frac{\partial \mathbf{g}}{\partial \mathbf{u}}$ is nearly constant and equal to **RNL**; therefore, the second derivative is zero. For this reason, we will refer to this formulation as SDF.

However, this assumption does not hold when the elements undergo finite deformation before failure. Therefore, one must modify the formulation when implementing the model for such applications. The following section will present the modifications implemented for cohesive zone elements undergoing finite deformation in modeling crazing in polymers.

2.1.1 Large Displacement Formulation

Element kinematics for finite deformation failure is not a very well-studied topic concerning CZMs. While few studies implement LDF for the bulk phases, models for finite deformation at the cohesive zone are fewer. Therefore, this subsection will present two formulations that deal with the main differences between SDF and LDF.

In connection to our discussion on the finite element formulation, the geometrical contribution to the stiffness is zero. However, as Reinoso and Paggi (2014) pointed out, this assumption is not valid when dealing with LDF. Therefore, they proposed additional terms for defining $\frac{\partial \mathbf{g}}{\partial \mathbf{u}}$ (eq. (2.15)) and the stiffness matrix (eq. (2.16)).

$$\frac{\partial \mathbf{g}}{\partial \mathbf{u}} = \mathbf{RNL} + \frac{\partial \mathbf{R}}{\partial \mathbf{u}}\mathbf{G} \tag{2.15}$$

$$\mathbf{K}^e = \int_{\xi_1,\xi_2} \left[\left(\frac{\partial^2 \mathbf{g}}{\partial \mathbf{u}^2} \right)^T \tau + \left(\frac{\partial \mathbf{g}}{\partial \mathbf{u}} \right)^T \frac{\partial \tau}{\partial \mathbf{g}} \left(\frac{\partial \mathbf{g}}{\partial \mathbf{u}} \right) \right] J d\mathbb{I}^e_{\xi_1,\xi_2} \tag{2.16}$$

The authors noted that the additional term in the stiffness matrix is not symmetric and therefore requires a non-symmetric solver (u). However, fig. 2.4 shows that omitting this term and using symmetric solver (s) does not significantly influence the load-displacement curves (fig. 2.4). Therefore, the authors ignored the unsymmetrical term in their series of studies implementing the finite displacement (Carollo et al. (2017), Paggi and Reinoso (2015), Reinoso and Paggi (2014), Reinoso et al. (2017a), Reinoso et al. (2017b)).

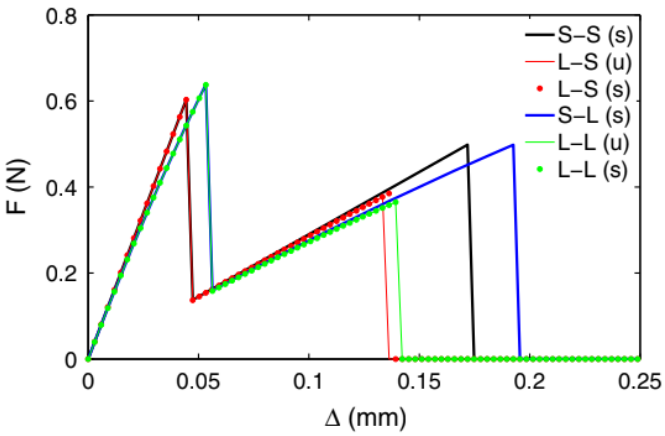

Figure 2.4: Load displacement curves from the numerical implementation of tension cut-off TSL with SDF(S) and LDF(L). Here X-Y indicates the formulation used for the cohesive zone and the bulk phase, and (x) denotes the solver type. (Reinoso and Paggi, 2014)

In their 2014 study, the authors showed that the formulation influences the load-displacement curves when implemented with non-uniform mixed-mode loading via single element simulations (Figure 2.5a) and peel test simulations (Figure 2.5c). However, they have not provided quantitative metrics comparing the LDF and SDF.

Further, one should note that this formulation only considers the geometric contributions of the large deformation to the finite element equation. The rotation vector is still defined using the mid-plane bases.

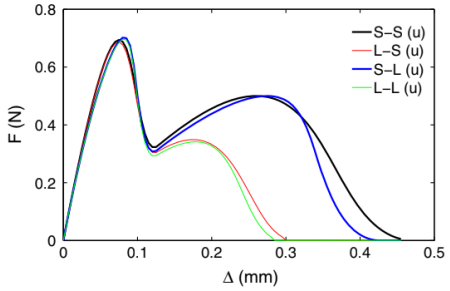

(a) Single element test with $\tau^I_{max}/\tau^{II}_{max} = 10$

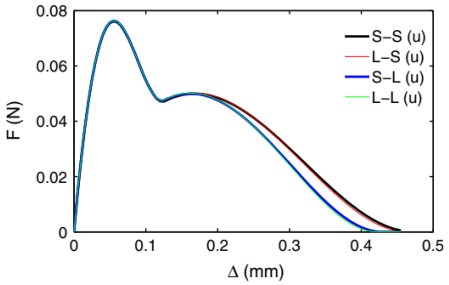

(b) Single element test with $\tau^I_{max}/\tau^{II}_{max} = 0.1$

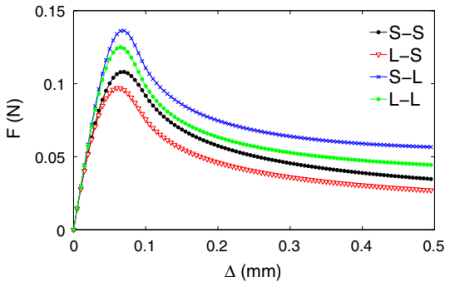

(c) Peel test

Figure 2.5: Load displacement curves from the numerical implementation of polynomial TSL with SDF(S) and LDF(L). Here X-Y indicates the formulation used for the cohesive zone and the bulk phase. (Reinoso and Paggi, 2014)

Contrary to that, Van den Bosch et al. (2007) postulate that the load-bearing capacity of the interface during crazing is due to the formation of fibrils that transfer load only along their natural axes. Therefore, they proposed a large deformation formulation that defines the local traction and separation at each integration point based on the local separation between the top and the bottom surfaces (fig. 2.6).

Such a formulation seems theoretically valid since the orientation of load-bearing fiber bridges that form during crazing depend on the top and the bottom surfaces independent of the mode ratio of applied loads. The authors showed that their formulation differed from the SDF using the dissipated energy (G_c) at a representative integration point and a correlation index between the load-displacement curves. However, Reinoso and Paggi (2014) pointed out that this formulation is not consistent with the geometric contributions to the finite element equation.

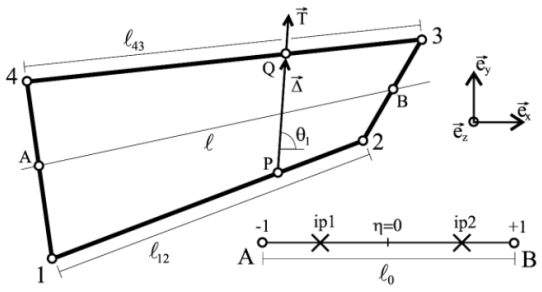

Figure 2.6: Two-dimensional four-node cohesive element with LDF as proposed by Van den Bosch et al. (2007)

It might be necessary to implement both the modifications for accurately modeling crazing. One can achieve this by **redefining the local basis vectors from eq. (2.6) to include the gap vector along with the mid-plane vectors and orthonormalizing them using the Gram–Schmidt process** as defined below:

$$\begin{aligned} \mathbf{e}_3 &= \frac{\mathbf{G}}{||\mathbf{G}||} \\ \mathbf{t}_1 &= \frac{\partial \mathbf{x_m}}{\partial \xi_1}, \quad \mathbf{p}_1 = \mathbf{t}_1 - Proj_{\mathbf{e}_3}(\mathbf{t}_1), \quad \mathbf{e}_1 = \frac{\mathbf{p_1}}{||\mathbf{p_1}||} \\ \mathbf{t}_2 &= \frac{\partial \mathbf{x_m}}{\partial \xi_2}, \quad \mathbf{p}_2 = \mathbf{t}_2 - Proj_{\mathbf{e}_3}(\mathbf{t}_2), \quad \mathbf{e}_2 = \frac{\mathbf{p_2}}{||\mathbf{p_2}||} \end{aligned} \tag{2.17}$$

where,

$$Proj_{\mathbf{u}}(\mathbf{v}) = \frac{\langle \mathbf{u}, \mathbf{v} \rangle}{\langle \mathbf{u}, \mathbf{u} \rangle} \mathbf{u}$$
$$\langle \mathbf{a}, \mathbf{b} \rangle = \mathbf{a} \bullet \mathbf{b}$$

An example of local basis thus determined at different locations along the mid-plane is shown in fig. 2.7

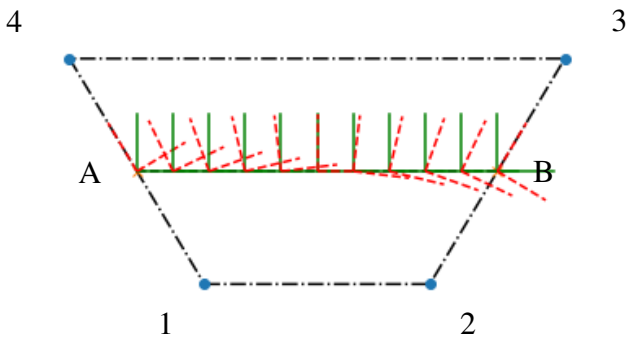

Figure 2.7: Two-dimensional four-node cohesive element. Here, — bases are defined based on the mid-plane & - - bases are defined using eq. (2.17)

Either definition of local bases requires careful calculation of the term $\frac{\partial \mathbf{R}}{\partial \mathbf{u}}\mathbf{G}$ when implementing Reinoso and Paggi (2014)'s nonlinear formulation. Appendix A presents the derivation of this quantity for both definitions of local bases, which completes the element formulation of the cohesive zone. The following section focuses on the constitutive relationship of the elements defined by the TSL.

2.1.2 Traction Separation Law

The TSL represents the relationship between the displacement gap $\mathbf{g}$ also referred to as Δ and a corresponding traction τ. We have come across some of these in fig. 2.1, which shows the schematic of three such TSLs, and fig. 2.4, fig. 2.5 present the load-displacement curves from mixed-mode simulations using tension cut-off and polynomial TSL, respectively.

Finite element formulation described previously can be implemented with these TSLs, and Park and Paulino (2011) reviewed some commonly used laws. Typically, to account for ductility in polymer interfaces, trapezoidal TSLs are used (Fernandes et al., 2016; De Moura et al., 2008). Recently, Jensen et al. (2019) proposed using multilinear laws to account for R-curve effects.

Nevertheless, the discussion in section 1.1 points out the requirement for further characterization of the formulation itself. The idea here is to choose a law that will allow for this characterization. By comparing fig. 2.4 and fig. 2.5a, one will notice that the law shape mainly influences the smoothness of the curve; however, both laws capture the difference between the SDF and LDF. Therefore to compare the formulation of the element kinematics, it is more important to use the same shape for both formulations than the shape itself.

Hence, the rest of this section focuses on bilinear TSL, also called the linear softening law, as it is simple to implement and used in simulating a wide variety of materials, including interfaces between viscoelastic bulk phases (Song et al., 2006) and metal-polymer bulk phases (Jang et al., 2017).

The law derives from the linear softening curve between damage onset and failure (Figure 2.8a). The bilinear law with quadratic interaction criterion ($\tau_m = \sqrt{\tau_s^2 + \tau_n^2}$, where $\tau_n = \tau_3$ is the traction in mode-I and $\tau_s = \sqrt{\tau_1^2 + \tau_2^2}$ is the traction in shear mode) as proposed by Camanho and Dávila (2002) and modified by Turon et al. (2006), is extremely popular for mixed-mode damage simulation.

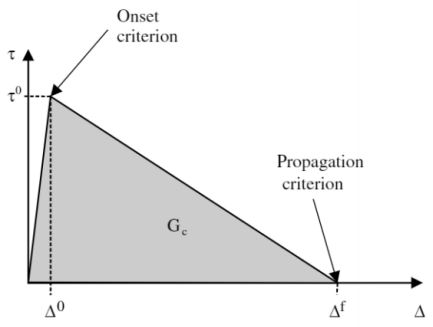

(a) TSL shape. (Turon et al., 2006)

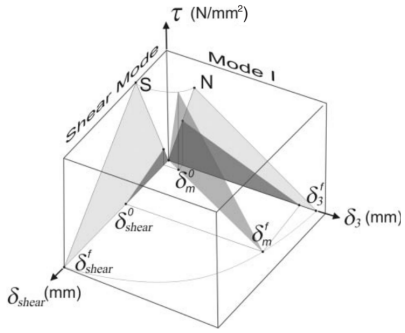

(b) Schematic of mixed-mode behavior. (Camanho et al., 2003)

Figure 2.8: Bilinear TSL

Turon et al. (2006) track the element damage (d) using the following equation,

$$d = \frac{\lambda_f \left(\lambda_m^{max} - \lambda_o\right)}{\lambda_m^{max} \left(\lambda_f - \lambda_o\right)} \tag{2.18}$$

derived from the maximum mixed-mode displacement jump (λ_m^{max}) undergone by the element until the current time. The mixed-mode displacement jump also has a quadratic relationship with the displacement tensor similar to the traction vector ($\lambda_m = \sqrt{g_1^2 + g_2^2 + g_3^2}$).

The quantities λ_o and λ_f defined below are the mixed-mode damage onset and failure separations.

$$\lambda_o = \sqrt{(g_3^o)^2 + \left((g_s^o)^2 - (g_3^o)^2\right) B^\eta} \tag{2.19}$$

$$\lambda_f = \frac{g_3^o g_3^f + \left(g_s^o g_s^f - g_3^o g_3^f\right) B^\eta}{\lambda_o} \tag{2.20}$$

λ_o and λ_f depend on the mixed-mode ratio (β) and the mixed-mode energy release ratio (B) as defined by the following equations:

$$\beta = \frac{g_s}{g_s + \langle g_3 \rangle} \tag{2.21}$$

$$B = \frac{\beta^2}{1 + 2\beta^2 - 2\beta} \tag{2.22}$$

where g_s is the separation in shear given by $\sqrt{g_1^2 + g_2^2}$, and $\langle \circ \rangle = \frac{1}{2}(\circ + |\circ|)$ is the MacAuley operator.

Turon et al. (2006) derived the expressions for mixed-mode separation limits (λ_o and λ_f) from normal (g_3^o and g_3^f) and shear mode (g_s^o and g_s^f) limits based on the Benzeggagh and Kenane (1996) energy release rate expression. The parameter η in eq. (2.19) and eq. (2.20) is the exponent from this mixed-mode law. Turon et al. (2006) express the constitutive relationship based on the quantities defined above with the following eq. (2.23) and 2.24

$$\tau = (1-d)\, K\mathbf{g} - dK \begin{bmatrix} 0 \\ 0 \\ \langle -g_3 \rangle \end{bmatrix} \tag{2.23}$$

$$\frac{\partial \tau_i}{\partial \mathbf{g_j}} = \begin{cases} D_{ij} - K\left[1 + \delta_{3j}\frac{\langle -g_j \rangle}{g_j}\right]\left[1 + \delta_{3i}\frac{\langle -g_i \rangle}{g_i}\right] H g_i g_j, & \lambda_m^{max} < \lambda_m < \Delta_f \\ D_{ij}, & \lambda_m < \lambda_m^{max} \text{ or } \Delta_f < \lambda_m \end{cases} \tag{2.24}$$

where K is the penalty stiffness, δ_{ij} is the Kronecker delta. Additionally,

$$H = \frac{\lambda_o \lambda_f}{\lambda_f - \lambda_o} \frac{1}{\lambda_m^3}, \quad \text{and}$$

$$D_{ij} = \delta_{ij} K \left[1 - d\left(1 + \delta_{3j}\frac{\langle -g_j \rangle}{g_j}\right)\right]$$

The set of equations (2.10, 2.23, 2.24, 2.14) completes the definition of the mixed-mode behavior for cohesive zone elements using a bilinear TSL. Since the aim is to characterize the mixed-mode response, the following section presents some standardized tests and corresponding analytical models.

2.2 Standardized Tests

Fracture mechanics is the study of how materials fail. The energy required per unit surface to cause a fracture in a material, also called toughness, is widely accepted as a metric for material resistance to fracture in the field of Fracture Mechanics. The simplified theory for rupture proposed by Griffith (1921), later modified by Irwin (1957) and Rice (1968), paved the basis for the field of fracture mechanics. The theory, now known as LEFM, deals with the mechanics of cracks and fractures in elastic bodies when the plastic zone ahead of the crack tip is smaller than the crack length.

As Arencón and Velasco (2009)'s interpretation of this theory posits that crack growth occurs near existing cracks and discontinuities within a material when the difference in the external work (W) and the elastically stored energy (U) is sufficient to compensate for the energy required to generate new surfaces.

$$\frac{dW}{da} - \frac{dU}{da} \geq \gamma \frac{dA}{da} \tag{2.25}$$

where γ is the surface free energy per unit area, dA is the associated surface increment, and a is the crack length.

Griffith (1921) and Irwin (1957) showed that this thermodynamic relation could predict stress intensity factors based on the specimen geometry, properties, and the applied load. When the stress factor exceeds a critical value, crack growth conditions are satisfied. Kanninen and Popelar (1985) proposed the compliance calibration method for estimating the strain energy release rate (SERR) of different specimen geometries using the Irwin-Kies equation in eq. (2.26).

$$G_T = \frac{P^2}{2B}\frac{dC}{da} \tag{2.26}$$

where G_T is the SERR, P is the force, B is the specimen thickness, C is the compliance ($\frac{P}{\delta}$), and a is the crack length.

While Kanninen and Popelar (1985) use a least-squares linear regression, typically, for beam-like specimens, compliance (C) is expressed using beam theories such as direct beam theory and corrected beam theory to determine closed-form expressions.

Reeder and Crews Jr (1990), Creton et al. (1992), Solly et al. (1995), Wang (1997), and Schnell et al. (1998) used analytical models developed based on this method with DCB, end notch flexure (ENF), ADCB, MMB, and other such specimen geometries for the experimental characterization of fracture toughness of polymer interfaces subjected to different modes of failure. Robinson et al. (2005), De Lorenzis and Zavarise (2008), Turon et al. (2018) are a few of many who used similar geometries for FE validation or characterization.

Additionally, Wang and Williams (1992) proposed the crack length correction factor Δ_I in eq. (2.27).

$$\begin{aligned} \Delta_I &= h\sqrt{\frac{E_1}{11G_{13}}\left[3 - 2\left(\frac{\Gamma}{1+\Gamma}\right)^2\right]} \\ \Gamma &= 1.18\frac{\sqrt{E_1E_2}}{G_{13}} \end{aligned} \tag{2.27}$$

Here E_1, E_2, and G_{13} are adherend engineering constants, and h is the adherend thickness, for DCB specimen to account for shear deformation and the rotation of the beams at the crack tip. Such rotation becomes significant when considering ductile interfaces that undergo large deformation. Davies et al. (1998) presented a survey of some of the popular tests for different failure modes and their analytical models with this correction factor.

Further, the fracture process zone might become considerably large where the LEFM is no longer applicable. Typically, theories based on J-R resistance or energy for fracture work replace the LEFM since these theories account for the plastic zone in the fracture process zone ahead of the crack tip (Arencón and Velasco, 2009). However, experimental characterization using these theories requires testing multiple specimens with varying crack geometries to estimate the fracture toughness. So instead, Da Silva et al. (2011) use another crack length correction term to account for the fracture process zone.

Chaves et al. (2014) presented a compilation of the analytical models for mixed-mode fracture characterization of ductile interfaces that undergo large deformations similar to the crazing mechanism discussed in section 1.2, considering the correction factors mentioned above. Based on Chaves et al. (2014)'s interpretation of the analytical models, Costa et al. (2017) performed an experimental campaign characterizing the mixed-mode fracture behavior of ductile adhesives using DCB, ENF, and MMB tests.

Additionally, Fernandes et al. (2016) characterized the influence of temperature on the mode-I and mode-II properties of one such ductile adhesive. Subsequently, Moreira et al. (2020) characterized the mixed-mode response of the adhesive used by Fernandes et al. (2016). However, they argued against MMB tests for ductile adhesives. The MMB tests proportionately combine the mode-I and mode-II loading conditions, as shown in fig. 2.9 into mixed-mode loading with a specific mode ratio. For the test specimen to experience the designed mode ratio, the load at $\frac{c+L}{L}P$ must remain perpendicular to the specimen length. Therefore, the specimen dimensions will have to be rather large when the interface undergoes large displacement before failure, requiring larger test equipment.

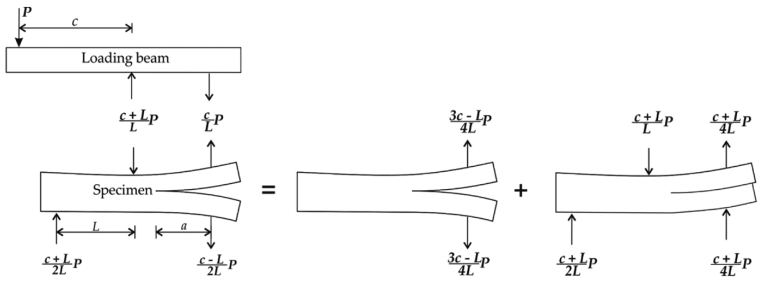

Figure 2.9: Effective modes in MMB tests Chaves et al. (2014)

Therefore, Moreira et al. (2020) proposed using ADCB, single-leg bending (SLB), and ASLB. These authors conducted mixed-mode tests with unidirectional carbon fiber reinforced plastics (CFRP) adherends using specimen schematics in fig. 2.10. Table 2.1 presents the engineering constants for the adherends, and table 2.2 presents the specimen dimensions used for different tests.

Further, to implement the cohesive zone model for the interface, along with the fracture properties in mode-I and mode-II derived from the DCB and ENF tests, one

E_{11} = 109 GPa	ν_{12} = 0.34	G_{12} = 4315 MPa
E_{22} = 8819 MPa	ν_{13} = 0.34	G_{13} = 4315 MPa
E_{33} = 8819 MPa	ν_{23} = 0.38	G_{23} = 3200 MPa

Table 2.1: Adhered properties from Moreira et al. (2020)

Specimen	Length (2L)	Thickness		Crack length (a_0)	G_{II}/G_C	G_C
		top (h_u)	bottom (h_l)			
DCB	100	2.4	2.4	40	0	0.42
ENF	200	2.4	2.4	80	1	4.2
ADCB	100	1.5	5.1	60	0.23	0.53
SLB	200	2.4	2.4	70	0.44	0.76
ASLB	200	2.4	5.1	70	0.34	0.62
ASLB	200	5.1	2.4	70	0.77	1.76

Table 2.2: Specimen dimensions and fracture properties from Moreira et al. (2020). All the specimens had 25mm width (B) and 0.2mm adhesive layer thickness (t)

needs the parameter for mixed-mode energy criteria similar to η in eq. (2.19) and (2.20). Ideally, one could find the parameter for the mixed-mode energy criteria by fitting criteria to the mixed-mode fracture toughnesses and the known mode ratios. However, for the ADCB and ASLB tests, the mode ratio cannot be estimated directly, unlike the MMB tests. Nevertheless, Moreira et al. (2020) showed that one could approximate the mode ratio using their MPM.

First, the authors simulated the mixed-mode tests assuming random values for the energy criteria parameter (γ). Then, using the force, displacement data from the simulations and analytical models presented in appendix B, the fracture resistance curves (r curves) can be determined. The plateaus in the r curves are the predicted fracture toughness values. A unique value for the mode ratio exists for each γ used and corresponding predicted fracture toughness.

The mode ratio is a metric for the energy release from different modes, and it turns out that for a given test, the unique values of the mode ratio corresponding to the fracture toughness predicted with different values of the γ are approximately the same, as indicated by fig. 2.11. Therefore, using this approach, one could estimate the mode ratio for mixed-mode tests. For example, the mode ratios and fracture toughness determined by Moreira et al. (2020) using the mode partitioning method for the ductile adhesive are in table 2.2.

Therefore, we can use these properties of the ductile adhesive and mixed-mode tests to compare the response of the SDF and LDF. However, in their FE implementations for the MPM, Moreira et al. (2020) used the power-law with parameter γ in place of the BK criteria implemented with TSL in section 2.1.2. Therefore, we must verify if the MPM results in similar predictions when implementing the FEM simulations with the BK-criterion instead of the power-law. The following section 2.3, presents the objectives for research based on this literature review.

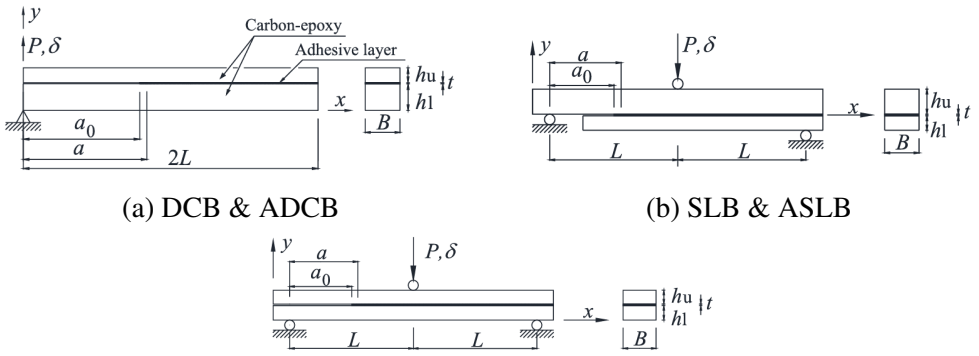

(a) DCB & ADCB

(b) SLB & ASLB

(c) ENF

Figure 2.10: Schematics for standard tests. (Moreira et al., 2020)

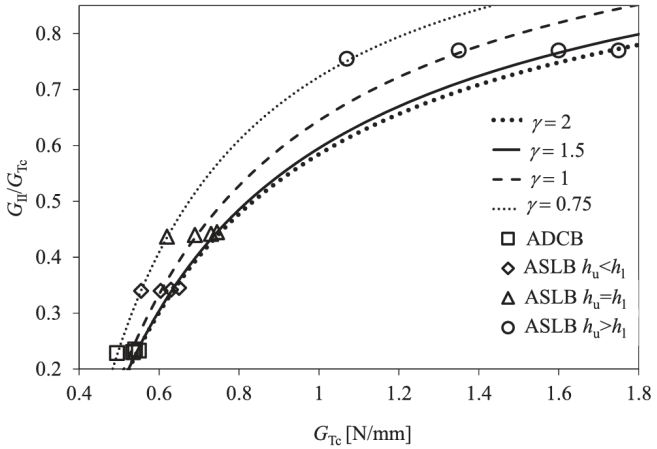

Figure 2.11: Mode ratio $\frac{G_{II}}{G_{T_C}}$ as a function of the total critical fracture toughness G_{T_C} (Moreira et al., 2020)

2.3 Research Objectives

As discussed in chapter 1, polymers undergo crazing during failure resulting in the formation of fibrils, and as a consequence, they undergo large deformation before failure (Kamei and Brown, 1984). Therefore, it is necessary to consider this behavior when modeling the interfaces in compatibilized polymer blends.

Reinoso and Paggi (2014) proposed an extended version of the cohesive zone element formulation accounting for material and geometric nonlinearities. However, based on their study on the response of single elements under predominantly mode-I load, they concluded that their formulation is only effective when the fracture properties of the interface are stronger in mode-I than the response in mode-II. Nevertheless, one might postulate that the inverse is true if the load case is predominantly mode-II. The latter scenario is relevant for modeling interfaces in polymer blends, as evidenced by several experimental studies showing that ductile polymers exhibit strong mode-II response (Wang, 1997).

In order to verify this hypothesis and validate the use of LDF to model the

interfaces in compatibilized polymer blends, we propose to characterize the response of the interfaces using both formulations under different cases of mixed mode loading.

Moreira et al. (2020) performed thorough experimental mixed-mode characterization of a ductile polymer adhesive using standardized tests. **Since ductile adhesives undergo crazing similar to polymers and block copolymers, we propose to use their test campaign as the basis to set up the finite element models for our simulation-based experimental work.**

Additionally, Moreira et al. (2020) proposed the mode partitioning method to estimate the mode ratio for the mixed-mode tests. They implemented the MPM with the power-law approximation of the fracture energies interactions. Since we implement the TSL with the BK criteria,

> **Our first objective is to replicate the conclusions from Moreira et al. (2020) with the BK criteria.**

If the method is replicable, we can conclude that the mode ratios estimated by Moreira et al. (2020) are accurate. Further,

> **We use the standardized tests and the fracture properties reported by Moreira et al. (2020) to compare the SDF and the LDF.**

Chapter 3 proposes the methodology to fulfill these objectives, starting with the test strategy for validating the MPM for BK criteria in section 3.1, followed by the test plan for comparing the SDF and LDF in section 3.2. Further, chapter 4 presents the results and discussion from the MPM, and chapter 5 compares the two cohesive element formulations. Finally, chapter 6 concludes this thesis with observations from the tests and recommendations for future work.

3 Methodology

This chapter presents the methodology and test plans to assess the validity of the mode partitioning method proposed by Moreira et al. (2020) in the following section 3.1. Further, section 3.2 presents the test plan to compare the small displacement formulation and the large displacement formulation under mixed-mode load.

3.1 Mode Partitioning Method

Moreira et al. (2020) proposed the MPM presented in section 2.2 to predict the mode ratio for mixed-mode tests. They predicted the mixed-mode fracture toughness and mode ratios using the MPM for a ductile polymer interface that undergoes large displacement and crazing similar to the PE-ipolypropylene (PP) interface. Therefore, simulating the mechanical behavior of this ductile interface using the SDF and the LDF would indicate whether or not the LDF is necessary to model ductile interfaces.

However, they implemented the MPM using the power-law as the mixed-mode energy criterion, unlike the BK energy criterion implemented with the TSL in section 2.1.2. Therefore, one of the objectives of this research is to determine if the BK criterion applies to the MPM. Additionally, since the mode ratio and fracture toughness in table 2.2 result from this method implemented with the power-law, we also need to determine if these values are law-specific or valid with the BK criterion.

To validate the use of the MPM with the BK criteria, we implement it to characterize the mode ratio of the ADCB test with specimen schematic shown in fig. 3.1. The elastic properties of the plies or the arms[1] with thickness h_u and h_l from table 2.1, and the parameters required to generate the computer-aided engineering (cae) model of the specimen are in table 3.1.

Additionally, although Moreira et al. (2020) used specimen width (B) 25 mm, the cae model in table 3.1 is of unit thickness to reduce the problem to a plain strain problem in 3D. The unit thickness model has only one element along the E2 direction. Next, plain strain conditions are imposed by fixing the E2 displacement of the faces with normals parallel to E_2. Further, the effective reaction forces for a specimen of required width W derives by increasing the simulation results W times, in this instance, 25 times.

[1] Hereinafter referred to as the bulk phase.

Parameter	Value	Mesh size
2L	100 mm	1 mm (excluding the crack)
a_0	60 mm	3 mm
t	0.2 mm	0.2 mm
B	1 mm	1 mm
h_u	1.5 mm	0.6 mm
h_l	5.1 mm	0.6 mm

Table 3.1: Parameters for the cae model of the ADCB test.

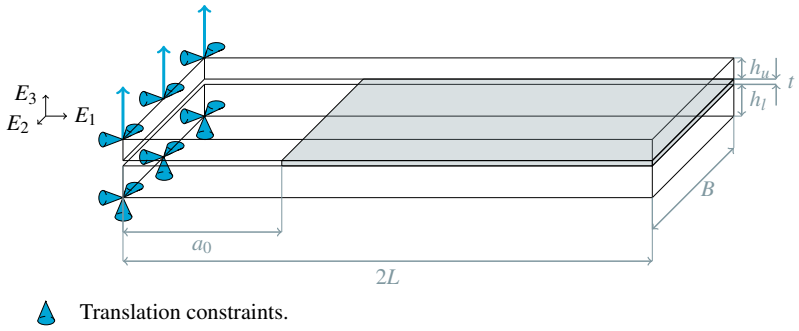

Figure 3.1: Schematic of the ADCB test specimen with boundary conditions.

Nevertheless, table 2.2 presents the mode-I and mode-II fracture toughness. We assume that the material is transversely isotropic with similar shear and sliding behavior. Therefore, the mode-III properties are the same as mode-II. Additionally, we assume a failure separation (Δ_f) of 0.2 mm for both failure modes. Since the model uses bilinear TSL, the nominal stress (τ_0) from fig. 2.8a can be derived using the following eq. (3.1).

$$G_x = \frac{1}{2}\Delta_{f_x}\tau_{0_x} \tag{3.1}$$

where x = I, II indicates the failure mode. Further, we must choose the initial penalty stiffness (K) carefully. Since the nominal stress (τ_0) and the separation at failure (Δ_f) are both fixed, the initial stiffness should be such that the displacement corresponding to separation at onset (Δ_o) is less than Δ_f.

$$K_x > \frac{2G_x}{\Delta_{f_x}^2}$$

Additionally, to ensure that the required time steps during the simulation are not too small, the Δ_o cannot be way too small. Considering these constraints, we use a penalty stiffness of 1250 N/mm, resulting in Δ_o of 0.0033 mm and 0.033 mm in modes - I and II, respectively. Finally, we sample the parameters γ or η for the power-law or the BK criteria using the Sobol sequence.

The design of this experiment assumes that all the material and model parameters are except the γ or η parameter. Hence, the independent variable for the experiments is the γ or the η parameter. The mode partitioning steps in section 3.1.1, implemented for each instance[2] of the designed experiments, predict corresponding mode-dependent fracture

[2]An instance is a single test case with all the fixed material and model parameters and one value from the sampled independent variable.

toughness and the mode ratio of the instance.

3.1.1 Steps to Implement The Mode Partitioning Method

1. Generate a cae model of the test specimen for the instance.
2. Run the finite element simulation of the model with Abaqus cae, 2018 to predict the reaction forces for applied displacements.
3. Convert the force-displacement data to r curves using the analytical models from appendix B.
4. Sample the fracture toughness values from the plateau region of the r curves.
5. Predict the mode ratios corresponding to the sampled fracture toughness values and the assumed γ or the η of the instance.
6. Determine the mean fracture toughness, mean predicted mode ratio, and the confidence intervals for the instance from the samples from steps 4 and 5.

Chapter 4 presents the results obtained using these steps for different values of γ and η, along with some observations on the predicted mode ratios. Finally, assuming that the data from table 2.1 is applicable with the BK criterion, section 3.2 presents the test plan for comparing the cohesive zone element formulations.

3.2 Small and Large Displacement Formulations

Reinoso and Paggi (2014) proposed the LDF to account for nonlinearities when cohesive zone elements undergo large deformation. However, they concluded that the formulation is not applicable for materials with stronger mode-II fracture properties based on predominantly mode-I load. Therefore the objective is to characterize the response of the SDF and the LDF for stronger mode-II materials under predominantly mode-II load. Since ductile polymer adhesives undergo crazing similar to the PE-iPP material system under consideration and also exhibit stronger mode-II fracture properties, section 3.2.1 presents the tests for characterizing the mixed-mode response of this material to replicate the experimental campaign by Moreira et al. (2020) with CFRP bulk.

Reinoso and Paggi (2014) performed peel tests using a stronger mode-I interface with both formulations. Since the bulk materials used in these tests had low elastic moduli, replicating these tests with a stronger mode-II interface will give insights into the influence of the nonlinearity at the interface induced by the bulk. Therefore, section 3.2.2 presents the schematic and the test conditions for the peel test with stronger mode-II interface.

Further, since the PE-iPP system is relatively similar to the low modulus system in the peel test as opposed to the CFRP bulk system, section 3.2.3 presents a test plan to investigate the influence of mode ratio on the response of the two formulations using the mixed-mode tests conducted by Moreira et al. (2020).

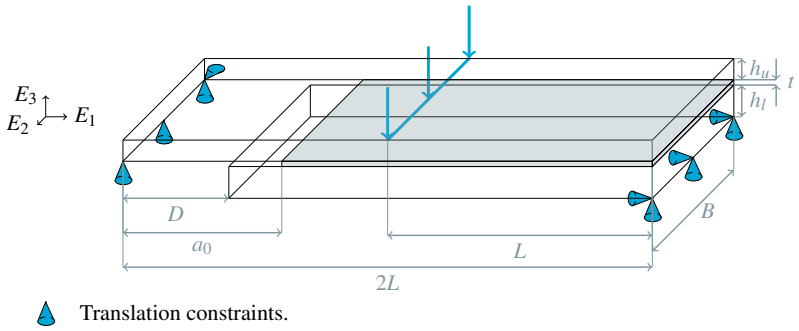

Figure 3.2: Schematic of the ASLB test specimen with boundary conditions.

3.2.1 Ductile Polymer Adhesive Interface

Section 3.1 presented the ADCB test for the CFRP + ductile polymer adhesive system. The ADCB test is a predominantly mode-I load case. Since a predominantly mode-II load case is required, this section focuses on the SLB test. However, the SLB test is a particular case of the ASLB test. Therefore, starting now, we refer to it as the ASLB test. Nevertheless, we use the material properties from table 2.1 as we did with the ADCB test. Further, the parameters required to generate the computer-aided engineering model of the specimen are in table 3.2, and the specimen geometry and boundary conditions are in fig. 3.2.

Parameter	Value	Mesh size
2L	200 mm	1 mm (excluding the crack)
a_0	70 mm	3 mm
t	0.2 mm	0.2 mm
B	1 mm	1 mm
h_u	2.4 mm	0.6 mm
h_l	2.4 mm	0.6 mm

Table 3.2: Parameters for the cae model of the ASLB test.

Additionally, the fracture toughness, penalty stiffness, and separation at failure (Δ_f) are similar to section 3.1. Moreover, assuming that the mode ratios and fracture toughness in table 2.1 are applicable for estimating the BK parameter, one could derive the η by fitting the BK criterion to the data. Chapter 5 first presents the results from the curve fitting and then the reaction-force predictions from the finite element implementation of the ASLB test with both the cohesive zone formulations using the η from the fitting process.

Further, since the CFRP bulk in these tests has high elastic moduli than the PE-iPP system, we also replicate the peel test conducted by Reinoso and Paggi (2014). However, we use a stronger mode-II interface instead. Following is section 3.2.2, presenting the peel test specifications.

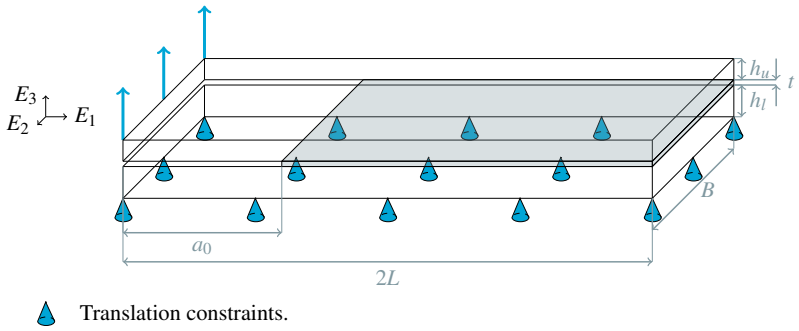

Figure 3.3: Schematic of the peel test specimen with boundary conditions.

3.2.2 Peel Test

Reinoso and Paggi (2014) performed the peel test using a back sheet with low modulus (E = 5 MPa) on a relatively rigid glass substrate with a stronger mode-I interface in between to compare the SDF and LDF. Therefore, the peel test uses a top ply with low modulus material with engineering constants from table 3.3 and bottom ply with CFRP properties from table 2.1. Further, table 3.4 presents the specimen dimensions, and the boundary conditions in fig. 3.3 effectively simulate the peel test.

$E_{11} = 5$ MPa	$\nu_{12} = 0.3$	$G_{12} = E_{11}/2(1+\nu_{12})$
$E_{22} = E_{11}$	$\nu_{13} = \nu_{12}$	$G_{13} = G_{12}$
$E_{33} = E_{11}$	$\nu_{23} = \nu_{12}$	$G_{23} = G_{12}$

Table 3.3: Elastic properties for the top ply in the peel test.

Parameter	Value	Mesh size
2L	50 mm	1 mm
a_0	1 mm	1 mm
t	0.001 mm	0.001 mm
B	1 mm	1 mm
h_u	0.2 mm	0.2 mm
h_l	5 mm	1 mm

Table 3.4: Parameters for the cae model of the peel test.

Note that the initial crack length is minimal to avoid excessive deformation in bulk ahead of the crack tip. Additionally, interfaces with fracture toughness as high as the ductile adhesive from the previous sections will also result in excessive deformation in the low modulus bulk. Therefore, Table 3.5 presents lower magnitude fracture properties for the cohesive zone assuming a Δ_f of 1 mm.

Case	K	G_{I_C}	G_{II_C}	τ_{O_I}	$\tau_{O_{II}}$	η
1	1	0.05	0.1	0.05	0.1	1
2	1	0.1	0.05	0.1	0.05	1

Table 3.5: Interface properties for the peel test.

Chapter 5 presents the results from these peel tests. Additionally, while the peel test is highly nonlinear, the applied loading from fig. 3.3 is still predominantly mode-I. Therefore, section 3.2.3 presents variations of the ADCB test to simulate different effective mode ratios.

3.2.3 Mixed-Mode Tests With Low Modulus Bulk

This section focuses on the tests for characterizing the mixed-mode response of specimens with low modulus bulk phases. Since the ADCB specimen gets its mixed-mode nature from the asymmetry in the arms, varying the thickness of the top ply (h_u) in comparison to the bottom ply (h_l) results in different effective mode ratios. Therefore, table 3.6 presents a set of test cases with varying h_u, and table 3.7 presents the remaining model parameters for the test schematic in fig. 3.1.

Case	h_u	Mesh size
1	3 mm	1 mm
2	5 mm	1 mm
3	8 mm	1 mm

Table 3.6: Test cases with varying top ply thickness (h_u) for the mixed-mode characterization.

Parameter	Value	Mesh size
2L	100 mm	1 mm
a_0	1 mm	1 mm
t	0.2 mm	0.2 mm
B	1 mm	1 mm
h_l	10 mm	1 mm

Table 3.7: Parameters for the cae model of the ADCB test.

Note that the bulk thicknesses in these ADCB specimens are higher than those previously used to avoid excessive deformation in bulk. Since the fracture toughness values in the peels tests are relatively low, thicker arms of the test specimen facilitate higher fracture toughness while avoiding excessive deformation in bulk Hence the increased thickness of the arms. Subsequently, the cohesive zone properties are also updated to the values in table 3.8, assuming a Δ_f of 2 mm for stronger mode-I and stronger mode-II interfaces.

K	G_{I_C}	G_{II_C}	τ_{O_I}	$\tau_{O_{II}}$	η
1	0.1	1	0.1	1	1

Table 3.8: Interface properties for the ADCB tests.

Additionally, both arms are low modulus materials with properties from table 3.3. Finally, chapter 5 presents the mode ratios from implementing the mode partition method in section 3.1 for these test cases.

The ADCB tests with varying energy criteria parameters compare the difference between the power-law and the BK criterion when implemented with the MPM. Additionally, the tests in section 3.2 characterize the influence of mode ratio, interface properties, and bulk properties on the difference between the two formulations. Appendix C presents the python script used in running the tests and the data from the tests. Finally, chapter 4 presents the results and observations on the mode partitioning method implemented with the power-law and the BK criterion, and chapter 5 compares the responses of the two formulations and recommendations on the use cases for the LDF based on these tests.

4 Mode Partitioning Method

This chapter compares the mode partitioning method implemented with the BK criteria and the power-law. First, section 4.1 presents sample results obtained from the MPM steps in section 3.1.1. Further, section 4.2 compares the predicted mode ratio and fracture toughness using the MPM with the power-law and the BK criteria.

4.1 MPM Implementation Example

This section presents the intermediate results obtained by implementing the steps of the MPM with the BK criteria assuming $\eta = 2.81$. First, step 1 in section 3.1.1 generates the ADCB specimen with geometry and material properties presented in section 3.1 along with the assumed η. As defined in step 2 of section 3.1.1, the finite element simulation of the cae model results in displacement and reaction force at the load end presented in fig. 4.1.

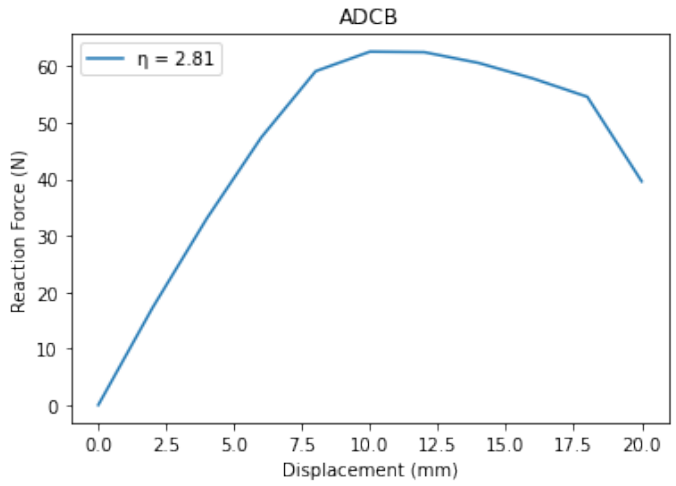

Figure 4.1: The magnitude of the displacement and reaction force at the load end of the ADCB test simulated using the FEM with the BK criteria.

Then, converting the displacement vs. reaction force data to effective crack length vs fracture resistance data using the analytical models in appendix B results in the fracture

resistance curve in fig. 4.2a. The plateau region in the fracture resistance curve is the critical fracture toughness for the test. Therefore, the plateau region sampled within limits as in fig. 4.2b is the fracture toughness. Figure 4.2b also presents the sample mean which is the mean predicted fracture toughness and the 95% confidence intervals.

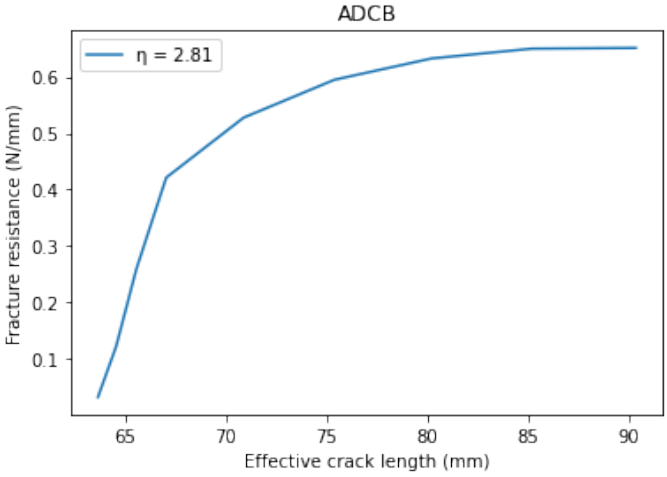

(a) Fracture resistance curve.

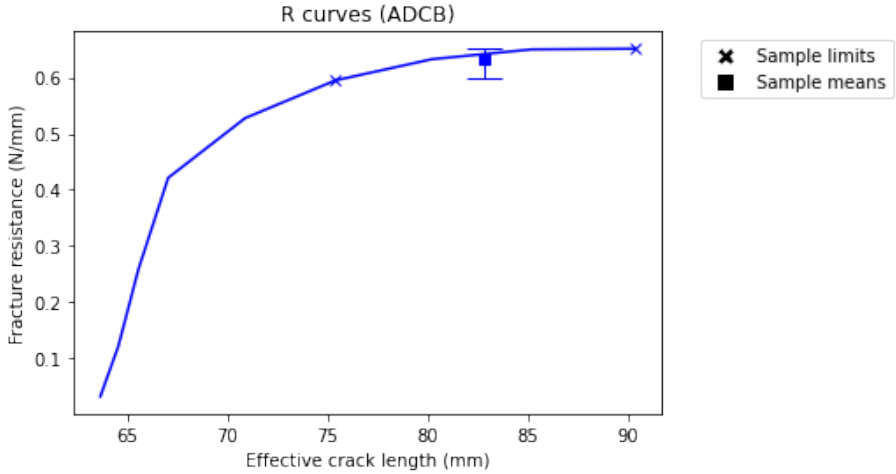

(b) Fracture toughness samples.

Figure 4.2: Fracture toughness of the ADCB test simulated using the FEM with the BK criteria.

Further, the BK criterion is eq. (4.1)

$$G_T = G_{IC} + (G_{IIC} - G_{IC})\, B^{\eta} \tag{4.1}$$

Since the critical fracture toughness in mode-I (G_{IC}) and mode-II (G_{IIC}), and the η are fixed for a given instance of the ADCB test, each value of mixed-mode fracture toughness sampled from fig. 4.2b results in a corresponding mode ratio (B). Finally, fig. 4.3 presents the sample mean and 95% confidence intervals of the predicted mode ratios and corresponding fracture toughness.

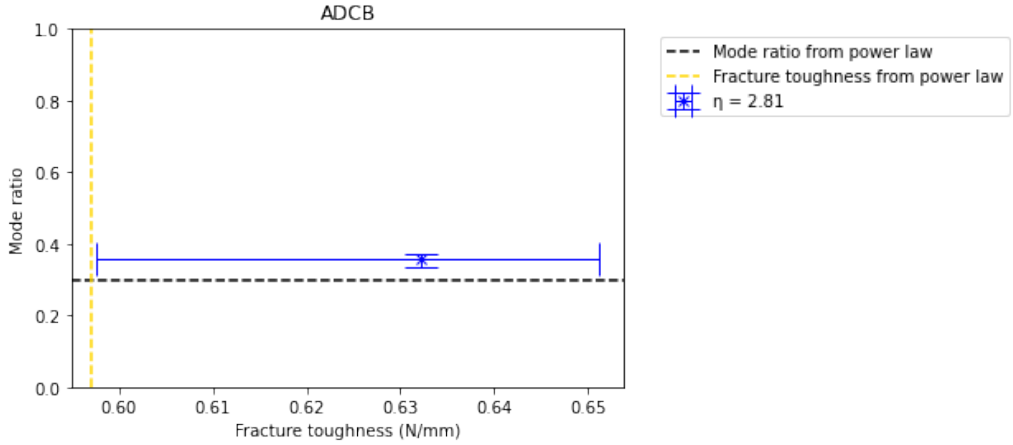

Figure 4.3: The fracture toughness and mode ratio predicted using the MPM for the ADCB test simulated using the FEM with the BK criteria.

According to Moreira et al. (2020), implementing the MPM with varying power-law should result in a similar estimate of the mode ratio. Therefore, Section 4.2 presents the mode ratios predicted using the MPM with the power-law and the BK criteria for varying γ and η to replicate Moreira et al. (2020)'s findings.

4.2 MPM With Power-law vs. BK Criteria

The mode partitioning steps implemented on the ADCB test using the power-law for five instances of γ selected between 1.5 and 2.5 using the Sobol sequence resulted in the mean predicted mode ratios in fig. 4.4.

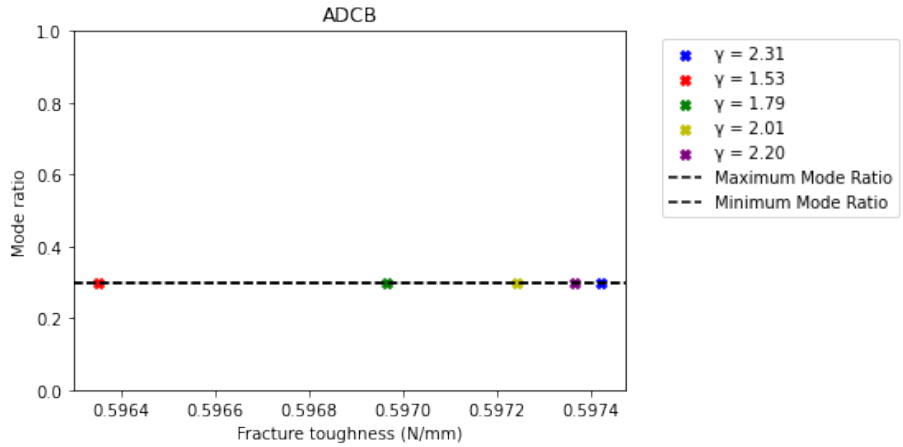

Figure 4.4: Mean predicted mode ratio of ADCB test from section 3.1 using MPM with power-law.

The predicted mode ratios from all the instances are approximately the same with a mean squared error of the order 10^{-7}. The predicted mode ratio and fracture toughness are slightly different from table 2.1. However, the difference could be due to slight differences

in the cae models used by Moreira et al. (2020) and the ones used here. Nevertheless, the predicted mode ratios and fracture toughness in fig. 4.4 are approximately the same. Therefore, we conclude that the MPM is replicable.

However, implementing a similar procedure with the BK criterion for ten instances of η between 1.5 and 2.5 results in the varying predictions of both the fracture toughness and mode ratio predictions as in fig. 4.5. Therefore, while further investigation is required for η and γ less than 1, the MPM works better with the power-law when the parameters are between 1.5 and 2.5.

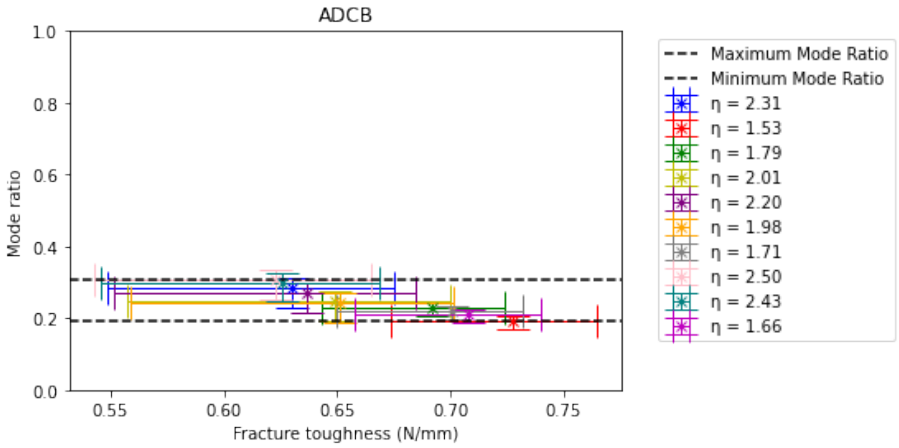

Figure 4.5: Mean predicted mode ratio of ADCB test from section 3.1 using mode partitioning method with the BK criterion.

Nevertheless, for some values of η, the mode ratio and fracture toughness predictions are close to the values obtained using the power-law as shown in fig. 4.6. While this does not confirm that the predictions from the mode partitioning method represent physical systems accurately, one could find η for the BK criteria to approximately replicate the response obtained using the power-law.

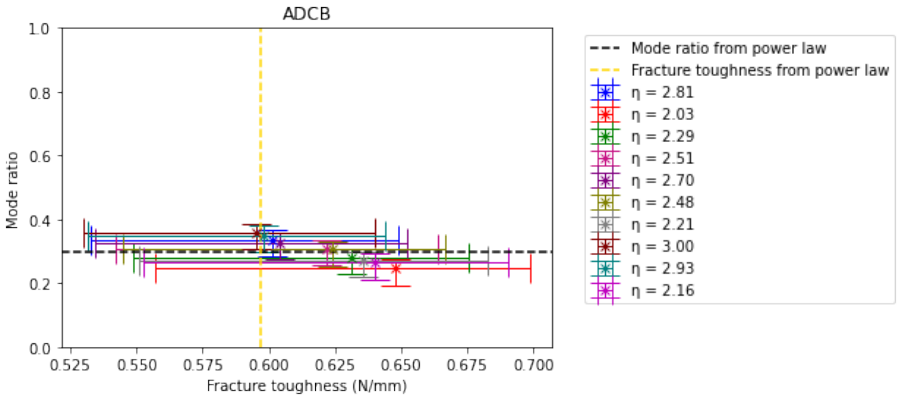

Figure 4.6: Mean predicted mode ratio of ADCB test from section 3.1 using mode partitioning method with the BK criterion.

The fracture toughness is predicted using the force-displacement data from the simulations. Therefore, to ensure that the predicted fracture toughness represents the

physical material system, one could find the most suitable γ and η by fitting the force-displacement data from simulations with the power-laws and the BK criteria to physical experimental results. Further, if the mode ratios predicted by this method using the γ and the η derived from the fitting process are approximately equal, one could conclude that the mode partitioning method is valid for characterizing the mode ratios for mixed-mode fracture tests. Additionally, implementing the MPM with MMB tests with predefined mode ratios could help validate the procedure. Nevertheless, one could obtain η to approximate the response of the power-law with the MPM. Therefore, the BK criterion could fit the fracture toughness and mode ratios in table 2.1 to find η for the CFRP + ductile polymer adhesive system.

5 Small Displacement Formulation vs. Large Displacement Formulation

This chapter focuses on the main objective of this work, i.e., comparing the influence of the mode ratio on the difference between the results from SDF and LDF assumptions for the cohesive zone elements. The ADCB test and the ASLB test with (h_u=h_l) as presented in section 3.2.1 are used to characterize the influence of mode ratio on the difference between two formulations for the CFRP + ductile adhesive system. However, this requires fitting the BK criterion to table 2.1 to determine the BK parameter for the cohesive zone, as mentioned in section 3.2.1 and chapter 4. Figure 5.1 presents the best fit BK criterion with $\eta = 3.71$.

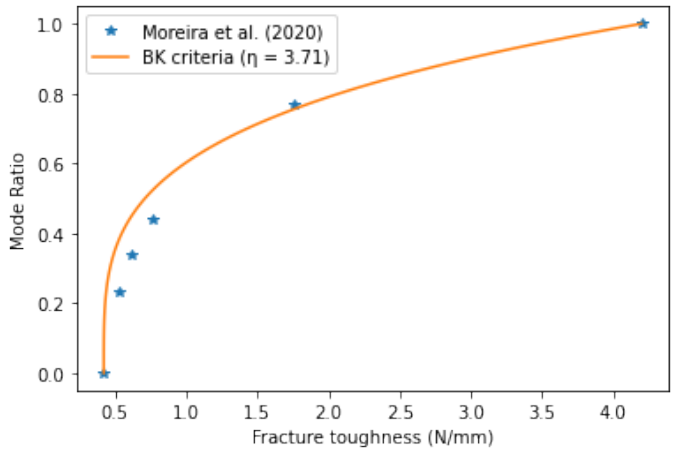

Figure 5.1: Best fit BK criterion for the data in table 2.1

5.1 Ductile Polymer Adhesive Interface

When implementing the models from section 3.2.1 with $\eta = 3.71$, if the hypothesis from section 1.3 were true, we would expect to see more prominent difference in the ASLB test than in the ADCB test. However, trials show no significant difference between the two formulations in either case as evidenced by fig. 5.2.

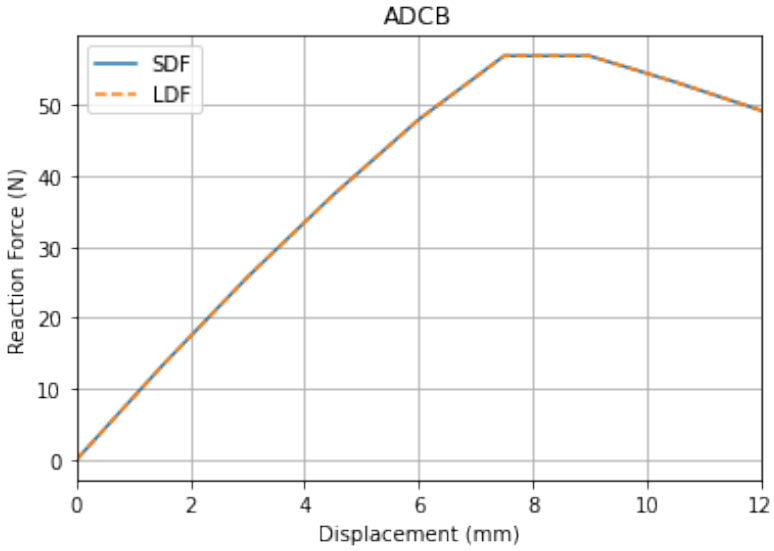

(a)

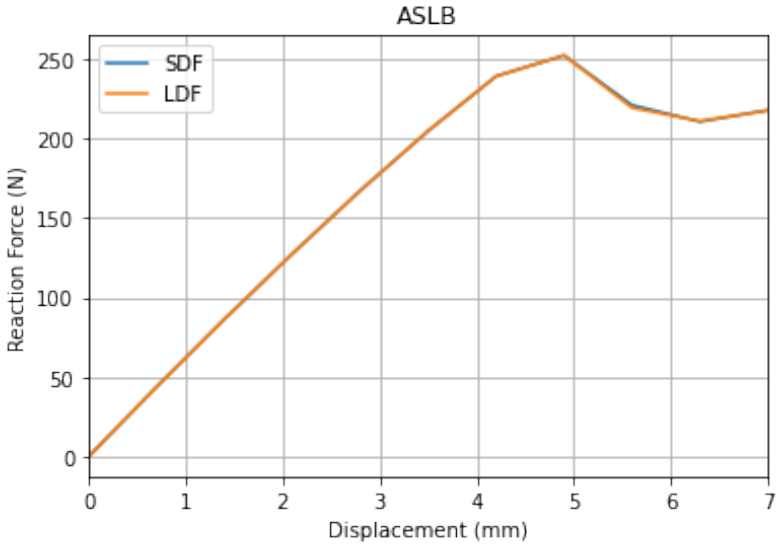

(b)

Figure 5.2: LDF vs. SDF with specimens and properties from section 3.2.1

Although this could confirm Reinoso and Paggi (2014)'s conclusions, running the same tests with stronger mode-I interface presented in fig. 5.3 indicates that the two formulations result in the same reaction force for stronger mode-I interface. However, Reinoso and Paggi (2014) already presented evidence that this is not the case using peel tests with low modulus bulk materials. Therefore, section 5.2 presents the results from peel tests conducted using the models from section 3.2.2 implemented with the CZM formulations.

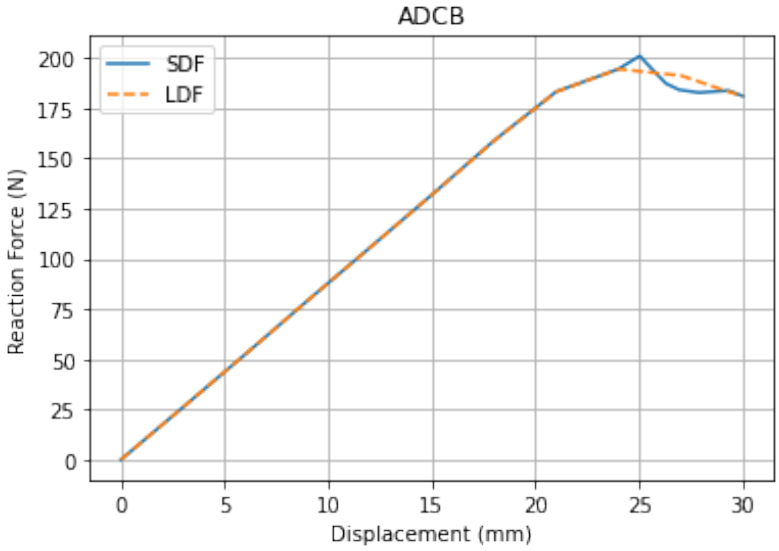

(a)

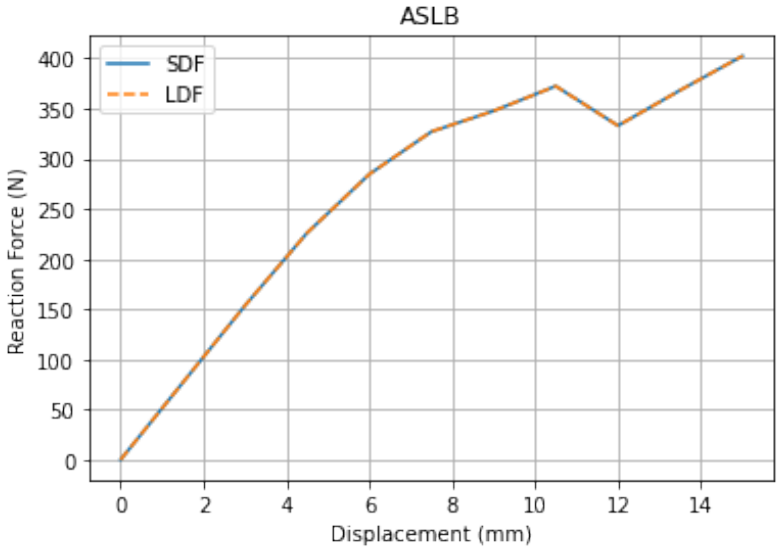

(b)

Figure 5.3: LDF vs. SDF for ADCB and ASLB tests with $G_{I_C} = 4.2$N/mm, and $G_{II_C} = 0.42$N/mm

5.2 Peel Tests

Section 3.2.2 presented peel tests with low modulus bulk materials. Running those tests showed that a stronger mode-I interface with $G_{I_C} = 0.1$ N/mm and $G_{II_C} = 0.05$ N/mm resulted in a difference in the forces from the two formulations as presented in fig. 5.4. Thereby replicating Moreira et al. (2020)'s results.

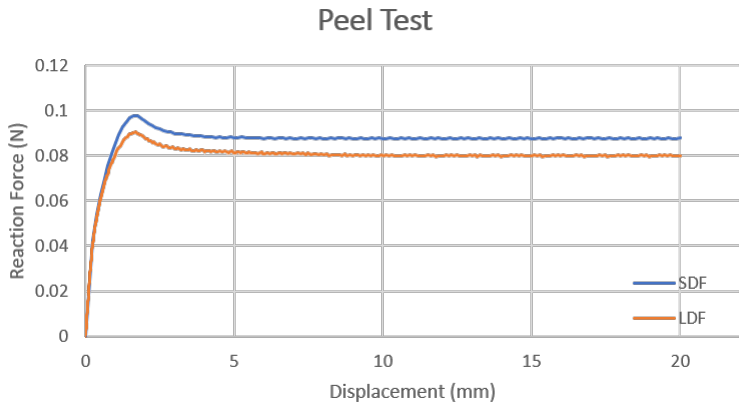

Figure 5.4: Peel tests results for LDF, SDF with $G_{I_C} = 0.1$ N/mm, and $G_{II_C} = 0.05$ N/mm

Additionally, simulations with stronger mode-II properties, i.e., $G_{I_C} = 0.05$ N/mm, and $G_{II_C} = 0.1$ N/mm, also result in a difference in the reaction forces from the two formulations as presented in fig. 5.5, indicating that the LDF influences the response for stronger mode-II materials. Moreover, for this particular load case, there a more significant difference between the LDF and the SDF in the case of stronger mode-I interfaces compared to stronger mode-II interfaces, indicating that the interface properties also influence the difference between the formulations.

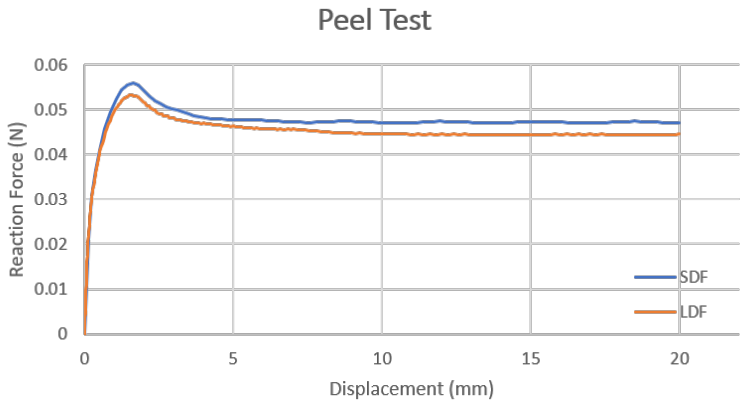

Figure 5.5: Peel tests results for LDF, SDF with $G_{I_C} = 0.05$ N/mm, and $G_{II_C} = 0.1$ N/mm

Furthermore, we note that only low modulus bulk materials result in these differences, unlike the stiff bulk materials such as the CFRP system in section 5.1. Therefore, the LDF is applicable at the cohesive zone for material systems with low modulus bulk phases that undergo large nonlinear deformations. That said, for the PE-iPP system under consideration, the stiffness of the bulk is not as high as CFRP. Therefore, the LDF will result in different responses than SDF. Hence section 5.3 revisits the mixed-mode tests with low modulus bulk materials to characterize the influence of the mode ratio on the difference between the two formulations and vice versa.

5.3 Mixed-Mode Tests With Low Modulus Bulk

The ADCB test presented in chapter 3 has boundary conditions similar to the mode-I DCB test. However, the asymmetry in the top and bottom bulk phases introduces some mode-II load, resulting in mixed-mode load at the interface. Therefore, section 3.2.3 proposed three configurations of the ADCB specimen with varying thickness of the top ply to characterize the influence of the mode ratio on the difference between the small displacement and large displacement formulations of the cohesive zone elements.

Further, a more considerable difference between the thickness of the top and bottom phases results in more influence from the shear mode. Therefore, since the specimens use bottom plies with h_l = 10 mm, top plies with h_u = 8 mm result in lower mode ratio loads than the tests with h_u = 3 mm. That said, fig. 5.6 presents the predicted fracture toughness and mode ratios determined using for these tests with different mode ratios and implementing the steps from section 3.1.1.

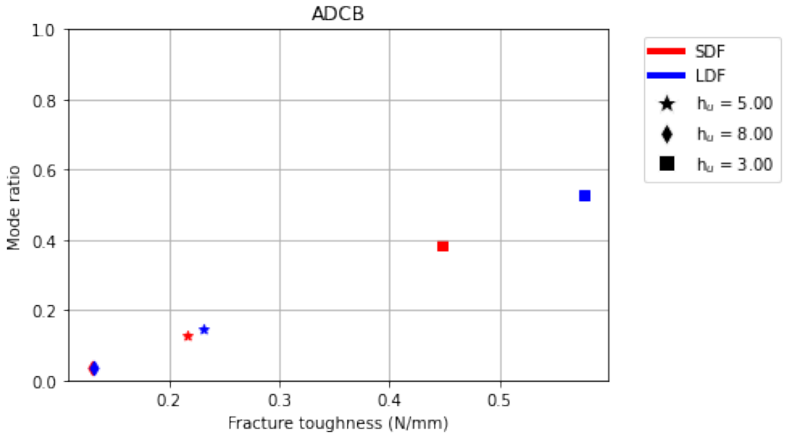

Figure 5.6: Peel tests results for LDF, SDF with $G_{I_C} = 0.05$ N/mm, and $G_{II_C} = 0.1$ N/mm

The difference between the mode ratios and fracture toughness predicted using the small displacement and the large displacement formulations increases as h_u decreases. Therefore, when used with stronger mode-II interfaces, the LDF has more influence on the response of the cohesive zone for load cases with more influence of shear mode confirming the hypothesis from section 1.3.

The specimen geometry, and consequently, the applied mode ratio directly influence the deformation ($\mathbf{u}$) of the interface and can be seen in fig. 5.7, where the interface undergoing predominantly mode-I load (fig. 5.7 A) experiences deformation primarily along the normal direction E_3, while the nodes undergo more deformation along E_1 as the influence of shear load increases.

Additionally, the LDF differs from the SDF in defining the $\frac{\partial \Delta}{\partial \mathbf{u}}$ term of the internal load and the tangent stiffness matrix of the finite element equation. Equation (2.15) shows that the LDF includes an additional term, the first derivative of the rotation matrix (dR^T) as defined in eq. (5.1), while the SDF assumes this term to be zero.

$$\frac{\partial \Delta}{\partial \mathbf{u}} = RNL + dR^T \tag{5.1}$$

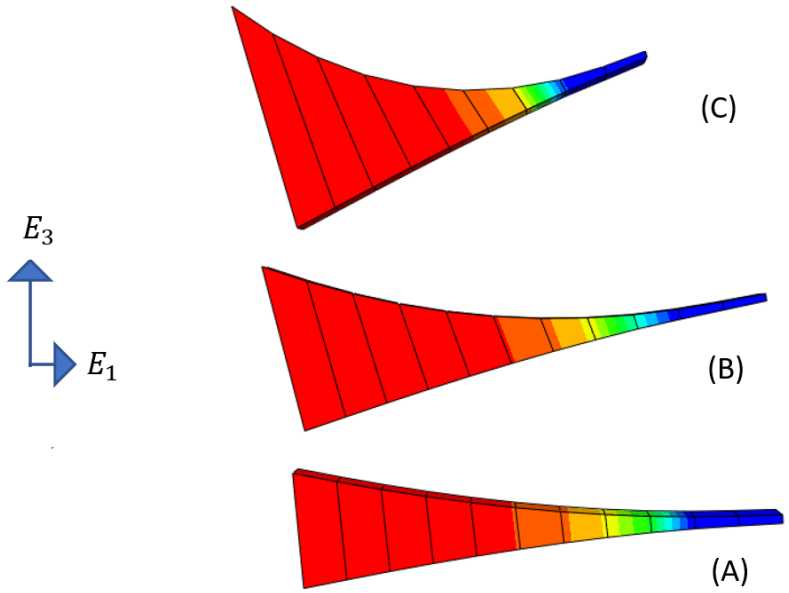

Figure 5.7: Deformed elements at the interface crack front with the gradients in damage variable (red = 1 fully damaged, blue = 0 undamaged) for (A) Test 1 with h_u=8, (B) Test 1 with h_u=5, (C) Test 1 with h_u=3.

Unlike Leibniz's notation, here dR^T denotes the additional term in eq. (2.15) that arises because the rotation matrix ($\mathbf{R}$) is dependent on the current deformation ($\mathbf{u}$), as defined in the following eq. (5.2) and x^T is the transpose of any matrix $\mathbf{x}$.

$$dR = \left(\frac{\partial \mathbf{R}}{\partial \mathbf{u}}\mathbf{NLU}\right)^T \tag{5.2}$$

The contribution from the LDF to the internal load derives from the product of $dR_{(24,3)}$ and the local traction ($\tau_{(3,1)}$). Here, $\mathbf{x}_{(m,n)}$ represents a matrix or a tensor $\mathbf{x}$ having m rows and n columns. Further, to investigate the cause for the observed influence of the applied mode ratio on the difference between the two formulations, figure 5 presents colormaps of the elements in these matrices (dR and τ) that correspond to a separation vector ($\Delta^{(e_i)}_{(3*1)}$) expressed in element local coordinates $e_{i=1,2,3}$ at a step time $t \cong 0.1$ sec extracted from the point $\xi_1 = -1$, $\xi_2 = 1$ of the element natural coordinate system for the first element of the interface at the crack front.

The rows 1 and 13 of columns 1 and 2 in the dR colormaps represent the influence of the deformation along E_1 of the top and bottom nodes close to the sampled integration point on the change of the orientation of the mid-plane defined by local basis $e_{i=1,2}$. Similarly, rows 3 and 15 of columns 1 and 2 in the dR colormaps represent the influence of the deformation along E_3. Further, column 3 represents the influence of deformation ($\mathbf{u}$) on the change in the orientation of local basis e_3.

From fig. 5.7, it is evident that the mid planes undergo more rotation for higher mode ratio test cases. Higher intensities of the elements in columns 1 and 2 of the dR colormaps from the higher mode ratio tests concur with this observation. Further, the intensities of the third column of dR are lower compared to the other columns, possibly because the tests are predominantly mode-I with large tensile loads applied along E_3, thereby

having smaller influence on the local basis e_3. Additionally, e_3 is the normal to the mid-plane. Therefore, the influence of the deformation vector ($\mathbf{u}$) and the mode ratio along e_3 are indirect. However, further investigation using predominantly mode-II load cases is required to verify this.

Nevertheless, from fig. 5.8a with negligible mode-II load, the smaller mode-I interface properties resulted in low magnitude traction coupled with low magnitudes of the column 3 elements in dR, resulting in an infinitesimal difference between the two formulations. On the other hand, higher intensities of the dR elements in columns 1 and 2 paired with higher traction in fig. 5.8b and 5.8c due to stronger mode-II properties,resulting in a more significant influence of the LDF over the response of the cohesive elements.

Nevertheless, there is enough evidence that the LDF results in a different response than the small displacement formulation under mixed-mode loading. Furthermore, the bulk phases undergo nonlinear deformation, and the interface properties in different modes are dissimilar and applicable to the compatibilized PE-iPP system. Finally, chapter 6 summarises this report with observations from chapter 4 and chapter 5.

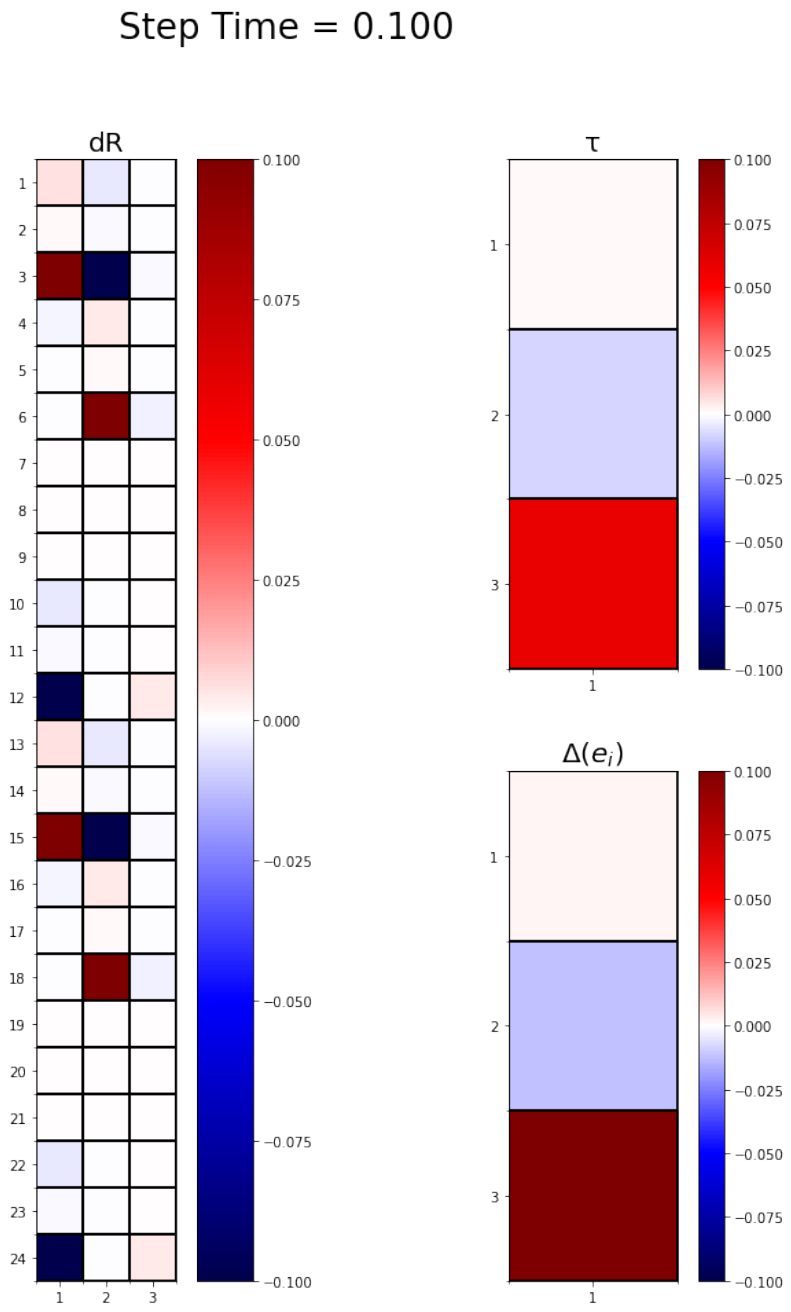

(a) Colormaps from ADCB test with $h_u = 8$.

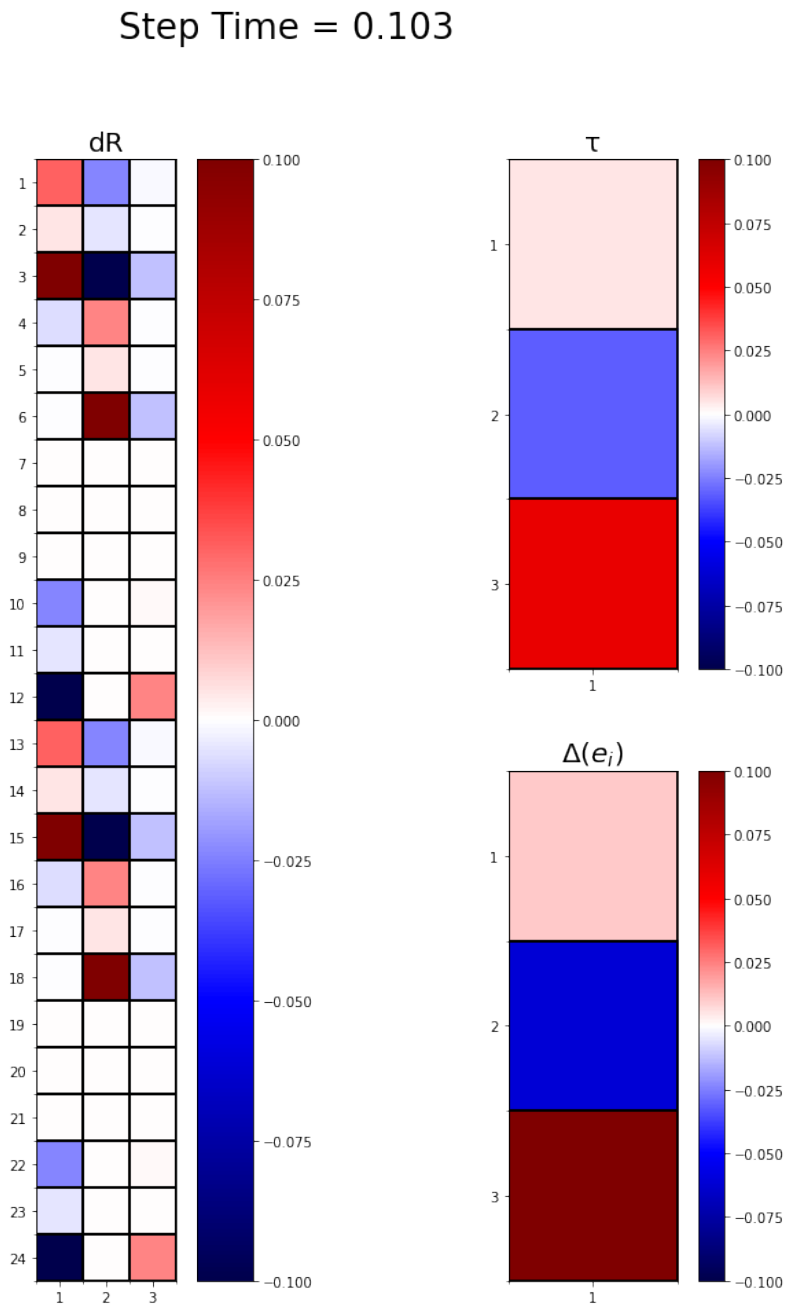

(b) Colormaps from ADCB test with $h_u = 5$.

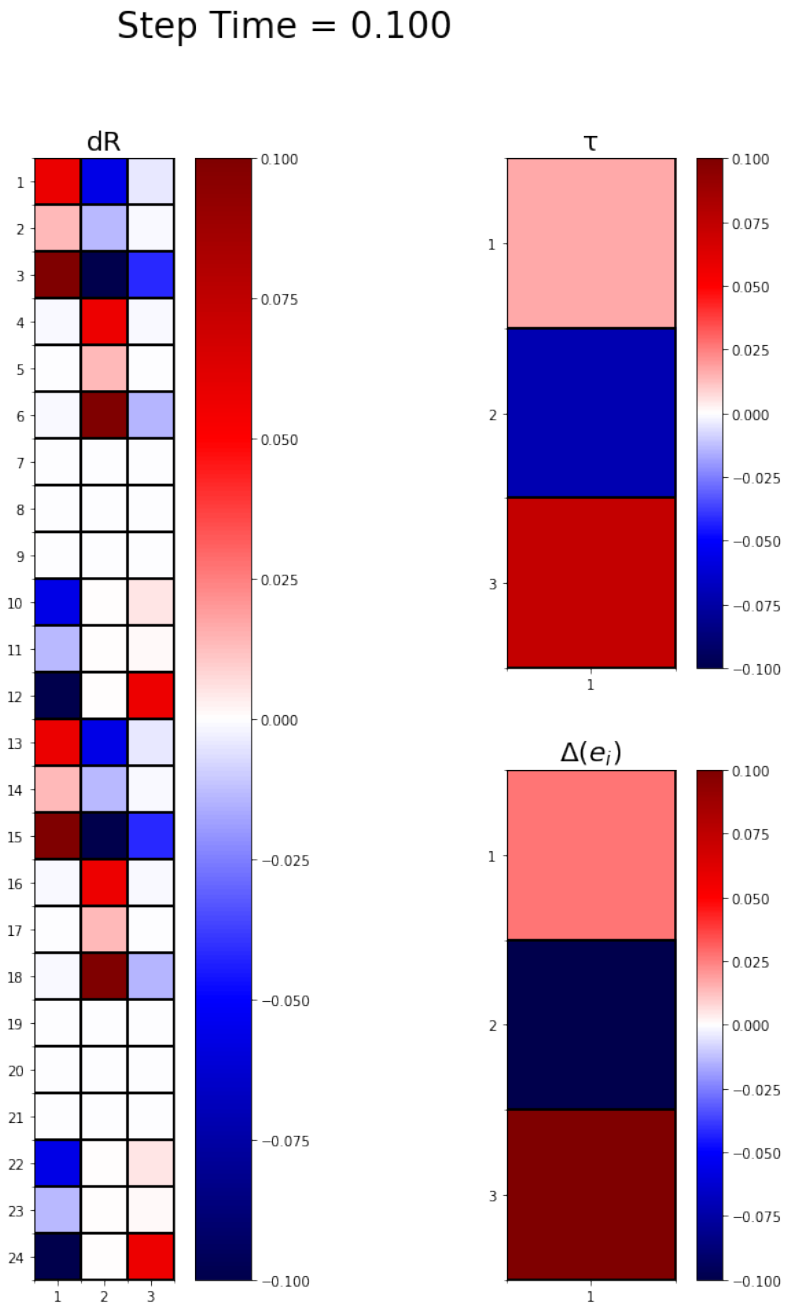

(c) Colormaps from ADCB test with $h_u = 3$.

Figure 5.8: Colormaps of elements in $dR_{(24,3)}$, $\tau_{(3,1)}$, and $\Delta_{(3,1)}$.

6 Conclusions & Recommendations

Plastic waste in landfills and the natural environment is a severe issue (Geyer et al., 2017). Of the lot, single-use plastics pose a higher threat due to smaller life cycles. Incompatibility between different types of plastics and difficulty in separation reduces the scope of recycling at the end of life. Dorigato (2021) and Eagan et al. (2017) showed that inherently incompatible plastics could be compatible with block copolymers. The use of compatibilizers removes the need for separation while enhancing the mechanical properties of polymer blends.

One could tailor the mechanical behavior of such composites using multiscale modeling (Llorca et al., 2013) or data-driven frameworks (Bessa et al., 2017). However, this requires careful validation of constituent phases in the blends. Furthermore, interface properties influence the system's behavior (Segurado and Llorca, 2005). Therefore, an appropriate model has to be used to model this behavior.

Since the failure zone is predefined, CZM is effective for modeling them. However, polymers undergo crazing during failure resulting in the formation of fibrils, and as a consequence, materials undergo large deformation before failure (Kamei and Brown, 1984). Reinoso and Paggi (2014) proposed an extended version of the cohesive zone element formulation to account for material and geometric nonlinearities. However, based on their study on the response of single elements under predominantly mode-I load, they concluded that their formulation is only effective when the fracture properties of the interface are stronger in mode-I than the response in mode-II.

Nevertheless, one might postulate that the inverse is true if the load case is predominantly mode-II. This scenario is relevant for modeling interfaces in polymer blends, as evidenced by several experimental studies, which show that ductile polymer interfaces exhibit strong mode-II response (Wang, 1997). Therefore, it is necessary to characterize the influence of the interface properties and the mode ratio on the response of the large displacement formulation to verify this hypothesis and validate the use of LDF to model the compatibilized polymer interfaces.

Moreira et al. (2020) performed thorough experimental mixed-mode characterization of a ductile polymer adhesive using standardized tests. They also proposed the mode partitioning method (MPM) to determine the mode ratios for tests in which this can not be determined directly. However, the MPM was implemented with the power-law as the mixed-mode energy criteria in place of the BK criteria presented in section 2.1.2. Implementing the MPM with the BK criteria resulted in a large difference between the

predicted mode ratios. Nevertheless, some values of the BK parameter η resulted in mode ratios and fracture toughness close to those predicted using the power-law.

Therefore, while the BK criteria may not be suitable for implementing the MPM, the results from the MPM implemented with the power-law could be used to fit the BK criteria.

Further, fitting the mixed-mode data presented by Moreira et al. (2020) and simulating these mixed-mode tests showed no influence of the LDF for the CFRP + ductile polymer adhesive system with stronger mode-II fracture toughness. However, when implemented for a stronger mode-I interface, there was no difference between the two formulations. On the contrary, Reinoso and Paggi (2014)'s peel tests showed that the two formulations are different for interfaces with stronger mode-I properties. Therefore, using similar peel tests with low modulus bulk phases and a stronger mode-II interface showed that the LDF responds differently to the SDF. However, the difference was not as prominent as running the peel test with a stronger mode-I interface.

Nevertheless, the LDF and the SDF resulted in different reaction forces when implemented with stronger mode-I and stronger mode-II interfaces. However, this is true when the bulk phases also undergo nonlinear deformation.

Moreover, simulating mixed-mode tests with stronger mode-II properties showed that as the influence of the stronger mode on the load case increases, the difference between the SDF and the LDF also increases, confirming the hypothesis that the mode ratio of the load case also influences the difference between the two formulations. While there is enough evidence to show that the LDF is also applicable for stronger mode-II interfaces, it is unknown whether if it is a better formulation to model materials undergoing large nonlinear deformation. Therefore, comparing the mixed-mode responses of the formulations and physical experiments.

Bibliography

D. Arencón and J. I. Velasco. Fracture toughness of polypropylene-based particulate composites. *Materials*, 2(4):2046–2094, 2009.

A. Argon, R. Cohen, B. Jang, and J. V. Sande. Crazing in two polystyrene/polybutadiene block copolymers. *Journal of Polymer Science: Polymer Physics Edition*, 19(2):253–272, 1981.

M. L. Benzeggagh and M. Kenane. Measurement of mixed-mode delamination fracture toughness of unidirectional glass/epoxy composites with mixed-mode bending apparatus. *Composites science and technology*, 56(4):439–449, 1996.

M. A. Bessa, R. Bostanabad, Z. Liu, A. Hu, D. W. Apley, C. Brinson, W. Chen, and W. K. Liu. A framework for data-driven analysis of materials under uncertainty: Countering the curse of dimensionality. *Computer Methods in Applied Mechanics and Engineering*, 320:633–667, 2017.

P. P. Camanho and C. G. Dávila. Mixed-mode decohesion finite elements for the simulation of delamination in composite materials. 2002.

P. P. Camanho, C. G. Davila, and M. De Moura. Numerical simulation of mixed-mode progressive delamination in composite materials. *Journal of composite materials*, 37 (16):1415–1438, 2003.

V. Carollo, J. Reinoso, and M. Paggi. A 3d finite strain model for intralayer and interlayer crack simulation coupling the phase field approach and cohesive zone model. *Composite Structures*, 182:636–651, 2017.

F. J. Chaves, L. Da Silva, M. De Moura, D. Dillard, and V. Esteves. Fracture mechanics tests in adhesively bonded joints: a literature review. *The Journal of Adhesion*, 90(12): 955–992, 2014.

M. Costa, R. Carbas, M. Benedita, E. Marques, G. Viana, L. Da Silva, E. Yokoi, S. Nakada, and T. Furusawa. Static assessment of the mixed-mode behaviour of three epoxy adhesives. *Engineering Fracture Mechanics*, 182:552–565, 2017.

C. Creton, E. J. Kramer, C. Y. Hui, and H. R. Brown. Failure mechanisms of polymer interfaces reinforced with block copolymers. *Macromolecules*, 25(12):3075–3088, 1992.

czmtestkit. Python package index for czmtestkit v1.0.0. URL `https://pypi.org/project/czmtestkit/`.

L. Da Silva, V. Esteves, and F. Chaves. Fracture toughness of a structural adhesive under mixed mode loadings. *Materialwissenschaft und Werkstofftechnik*, 42(5):460–470, 2011.

P. Davies, B. Blackman, and A. Brunner. Standard test methods for delamination resistance of composite materials: current status. *Applied composite materials*, 5(6): 345–364, 1998.

L. De Lorenzis and G. Zavarise. Modeling of mixed-mode debonding in the peel test applied to superficial reinforcements. *International Journal of Solids and Structures*, 45(20):5419–5436, 2008.

M. De Moura, R. Campilho, and J. Gonçalves. Crack equivalent concept applied to the fracture characterization of bonded joints under pure mode i loading. *Composites Science and Technology*, 68(10-11):2224–2230, 2008.

A. M. Donald and E. J. Kramer. Craze initiation and growth in high-impact polystyrene. *Journal of Applied Polymer Science*, 27(10):3729–3741, 1982.

A. Dorigato. Recycling of polymer blends. *Advanced Industrial and Engineering Polymer Research*, 2021.

J. M. Eagan, J. Xu, R. Di Girolamo, C. M. Thurber, C. W. Macosko, A. M. LaPointe, F. S. Bates, and G. W. Coates. Combining polyethylene and polypropylene: Enhanced performance with pe/ipp multiblock polymers. *Science*, 355(6327):814–816, 2017.

M. Elices, G. Guinea, J. Gomez, and J. Planas. The cohesive zone model: advantages, limitations and challenges. *Engineering fracture mechanics*, 69(2):137–163, 2002.

R. Fernandes, M. De Moura, and R. Moreira. Effect of temperature on pure modes i and ii fracture behavior of composite bonded joints. *Composites Part B: Engineering*, 96: 35–44, 2016.

E. García-Macías, C. F. Guzmán, E. I. S. Flores, and R. Castro-Triguero. Multiscale modeling of the elastic moduli of cnt-reinforced polymers and fitting of efficiency parameters for the use of the extended rule-of-mixtures. *Composites Part B: Engineering*, 159:114–131, 2019.

R. Geyer, J. R. Jambeck, and K. L. Law. Production, use, and fate of all plastics ever made. *Science advances*, 3(7):e1700782, 2017.

C. Gonzalez and J. Llorca. Multiscale modeling of fracture in fiber-reinforced composites. *Acta materialia*, 54(16):4171–4181, 2006.

A. A. Griffith. Vi. the phenomena of rupture and flow in solids. *Philosophical transactions of the royal society of london. Series A, containing papers of a mathematical or physical character*, 221(582-593):163–198, 1921.

G. R. Irwin. Analysis of stresses and strains near the end of a crack traversing a plate. 1957.

B. Jang, D. R. Uhlmann, and J. Vander Sande. Crazing in polypropylene. *Polymer Engineering & Science*, 25(2):98–104, 1985.

J. Jang, M. Sung, S. Han, and W.-R. Yu. Prediction of delamination of steel-polymer composites using cohesive zone model and peeling tests. *Composite Structures*, 160: 118–127, 2017.

S. M. Jensen, M. Martos, B. L. V. Bak, and E. Lindgaard. Formulation of a mixed-mode multilinear cohesive zone law in an interface finite element for modelling delamination with r-curve effects. *Composite Structures*, 216:477–486, 2019.

E. Kamei and N. Brown. Crazing in polyethylene. *Journal of Polymer Science: Polymer Physics Edition*, 22(4):543–559, 1984.

M. F. Kanninen and C. L. Popelar. Advanced fracture mechanics. 1985.

H. Kausch, J.-L. Halary, and C. Plummer. Crazing and fracture in polymers: Micromechanisms and effect of molecular variables. In *Macromolecular Symposia*, volume 214, pages 17–30. Wiley Online Library, 2004.

B. Koltisko, A. Hiltner, E. Baer, and L. Tung. Crazing in thin films of styrene–butadiene–styrene block copolymers. *Journal of Polymer Science Part B: Polymer Physics*, 24 (10):2167–2183, 1986.

E. J. Kramer and L. L. Berger. Fundamental processes of craze growth and fracture. In *Crazing in Polymers Vol. 2*, pages 1–68. Springer, 1990.

B. D. Lauterwasser and E. J. Kramer. Microscopic mechanisms and mechanics of craze growth and fracture. *Philosophical Magazine A*, 39(4):469–495, 1979.

D. Legrand. Crazing, yielding, and fracture of polymers. i. ductile brittle transition in polycarbonate. *Journal of applied polymer science*, 13(10):2129–2147, 1969.

C. Li and T.-W. Chou. Multiscale modeling of compressive behavior of carbon nanotube/polymer composites. *Composites science and technology*, 66(14):2409–2414, 2006.

X. Liu, T. Tang, W. Yu, and R. B. Pipes. Multiscale modeling of viscoelastic behaviors of textile composites. *International Journal of Engineering Science*, 130:175–186, 2018.

J. Llorca, C. González, J. Molina-Aldareguía, and C. Lopes. Multiscale modeling of composites: toward virtual testing... and beyond. *Jom*, 65(2):215–225, 2013.

A. Lustiger and R. Corneliussen. The role of crazes in the crack growth of polyethylene. *Journal of materials Science*, 22(7):2470–2476, 1987.

G. Marshall, L. Culver, and J. G. Williams. Craze growth in polymethylmethacrylate: a fracture mechanics approach. *Proceedings of the Royal Society of London. A. Mathematical and Physical Sciences*, 319(1537):165–187, 1970.

R. Moreira, M. de Moura, F. Silva, F. Ramírez, and J. Rodrigues. Mixed-mode i+ ii fracture characterisation of composite bonded joints. *Journal of Adhesion Science and Technology*, 34(13):1385–1398, 2020.

M. Paggi and J. Reinoso. An anisotropic large displacement cohesive zone model for fibrillar and crazing interfaces. *International Journal of Solids and Structures*, 69:106–120, 2015.

K. Park and G. H. Paulino. Cohesive zone models: a critical review of traction-separation relationships across fracture surfaces. *Applied Mechanics Reviews*, 64(6), 2011.

A. Pineau. Modeling ductile to brittle fracture transition in steels—micromechanical and physical challenges. *International Journal of Fracture*, 150(1-2):129–156, 2008.

J. R. Reeder and J. H. Crews Jr. Mixed-mode bending method for delamination testing. *AiAA Journal*, 28(7):1270–1276, 1990.

J. Reinoso and M. Paggi. A consistent interface element formulation for geometrical and material nonlinearities. *Computational Mechanics*, 54(6):1569–1581, 2014.

J. Reinoso, M. Paggi, and A. Blázquez. A nonlinear finite thickness cohesive interface element for modeling delamination in fibre-reinforced composite laminates. *Composites Part B: Engineering*, 109:116–128, 2017a.

J. Reinoso, M. Paggi, and C. Linder. Phase field modeling of brittle fracture for enhanced assumed strain shells at large deformations: formulation and finite element implementation. *Computational Mechanics*, 59(6):981–1001, 2017b.

J. R. Rice. A path independent integral and the approximate analysis of strain concentration by notches and cracks. 1968.

P. Robinson, U. Galvanetto, D. Tumino, G. Bellucci, and D. Violeau. Numerical simulation of fatigue-driven delamination using interface elements. *International journal for numerical methods in engineering*, 63(13):1824–1848, 2005.

R. Schnell, M. Stamm, and C. Creton. Direct correlation between interfacial width and adhesion in glassy polymers. *Macromolecules*, 31(7):2284–2292, 1998.

J. Segurado and J. Llorca. A computational micromechanics study of the effect of interface decohesion on the mechanical behavior of composites. *Acta materialia*, 53 (18):4931–4942, 2005.

R. K. Solly et al. Adhesive repair of carbon-fibre composite panel delaminations. In *NATIONAL CONFERENCE PUBLICATION-INSTITUTION OF ENGINEERS AUSTRALIA NCP*, pages 823–828. Institution of Engineers, Australia, 1995.

S. H. Song, G. H. Paulino, and W. G. Buttlar. A bilinear cohesive zone model tailored for fracture of asphalt concrete considering viscoelastic bulk material. *Engineering Fracture Mechanics*, 73(18):2829–2848, 2006.

M. Tijssens, E. Van der Giessen, and L. Sluys. Modeling of crazing using a cohesive surface methodology. *Mechanics of Materials*, 32(1):19–35, 2000.

A. Turon, P. P. Camanho, J. Costa, and C. Dávila. A damage model for the simulation of delamination in advanced composites under variable-mode loading. *Mechanics of materials*, 38(11):1072–1089, 2006.

A. Turon, E. González, C. Sarrado, G. Guillamet, and P. Maimí. Accurate simulation of delamination under mixed-mode loading using a cohesive model with a mode-dependent penalty stiffness. *Composite Structures*, 184:506–511, 2018.

M. Van den Bosch, P. Schreurs, and M. Geers. A cohesive zone model with a large displacement formulation accounting for interfacial fibrilation. *European Journal of Mechanics-A/Solids*, 26(1):1–19, 2007.

C. Wang. Fracture of interface cracks under combined loading. *Engineering fracture mechanics*, 56(1):77–86, 1997.

Y. Wang and J. Williams. Corrections for mode ii fracture toughness specimens of composites materials. *Composites Science and Technology*, 43(3):251–256, 1992.

Z. Xia, W. Curtin, and P. Peters. Multiscale modeling of failure in metal matrix composites. *Acta Materialia*, 49(2):273–287, 2001.

D.-B. Xu, C.-Y. Hui, E. Kramer, and C. Creton. A micromechanical model of crack growth along polymer interfaces. *Mechanics of Materials*, 11(3):257–268, 1991.

X.-P. Xu and A. Needleman. Numerical simulations of fast crack growth in brittle solids. *Journal of the Mechanics and Physics of Solids*, 42(9):1397–1434, 1994.

A Partial Derivative of the Local Separation

This appendix chapter presents the method for deriving the partial derivative of local separation for LDF proposed by Reinoso and Paggi (2014). This quantity requires the derivation of $\frac{\partial \mathbf{R}}{\partial \mathbf{u}}\mathbf{G}$. As the transformation matrix $\mathbf{R}$ gathers the local bases, so does its partial derivative as in eq. (A.2). Here, subscripts indicate the dimensions of the matrices or tensors.

$$\left[\frac{\partial \mathbf{R}}{\partial \mathbf{u}}\mathbf{G}\right]_{3\times 24} = \frac{\partial \mathbf{R}_{3\times 3}}{\partial \mathbf{u}_{24\times 1}}\mathbf{G}_{3\times 1} = \left[\frac{\partial \mathbf{R}}{\partial u_j}\mathbf{G}\right] \quad j = 1,24 \tag{A.1}$$

where,

$$\frac{\partial \mathbf{R}_{3\times 3}}{\partial u_j}\mathbf{G}_{3\times 1} = \frac{\partial}{\partial u_j}\left[\mathbf{e}_i^T\right]\mathbf{G} = \left[\frac{\partial \mathbf{e}_i^T}{\partial u_j}\right]\mathbf{G} \quad i = 1,2,3 \tag{A.2}$$

Partial derivatives of the local bases depend on the definition of the bases (eq. (2.6), eq. (2.17)). Derivation of these partials derivatives only requires the following set of expressions:

For vectors **a**,**b**;

- if $\mathbf{a} = \dfrac{\mathbf{b}}{||\mathbf{b}||}$

  then, $$\frac{\partial \mathbf{a}}{\partial x} = \frac{||\mathbf{b}||\frac{\partial \mathbf{b}}{\partial x} - \mathbf{b}\frac{\partial ||\mathbf{b}||}{\partial x}}{||\mathbf{b}||^2}$$

  where, $$\begin{aligned}\frac{\partial ||\mathbf{b}||}{\partial x} &= \frac{\partial \sqrt{\langle \mathbf{b},\mathbf{b}\rangle}}{\partial x} \\ &= \frac{\langle \mathbf{b}, \frac{\partial \mathbf{b}}{\partial x}\rangle + \langle \frac{\partial \mathbf{b}}{\partial x}, \mathbf{b}\rangle}{2||\mathbf{b}||} \\ &= \frac{\langle \mathbf{b}, \frac{\partial \mathbf{b}}{\partial x}\rangle}{||\mathbf{b}||}\end{aligned}$$

- $\dfrac{\partial\langle \mathbf{a},\mathbf{b}\rangle}{\partial x} = \langle \mathbf{a}, \dfrac{\partial \mathbf{b}}{\partial x}\rangle + \langle \dfrac{\partial \mathbf{a}}{\partial x}, \mathbf{b}\rangle$
- $\dfrac{\partial \mathbf{a}\times\mathbf{b}}{\partial x} = \mathbf{a}\times\dfrac{\partial \mathbf{b}}{\partial x} + \dfrac{\partial \mathbf{a}}{\partial x}\times\mathbf{b}$
- $\dfrac{\partial Proj_{\mathbf{a}}(\mathbf{b})}{\partial x} = \dfrac{\langle \mathbf{a},\mathbf{b}\rangle \frac{\partial \mathbf{a}}{\partial x} + \frac{\partial\langle \mathbf{a},\mathbf{b}\rangle}{\partial x}\mathbf{a}}{\langle \mathbf{a},\mathbf{a}\rangle} - \dfrac{\partial\langle \mathbf{a},\mathbf{a}\rangle}{\partial x}\dfrac{Proj_{\mathbf{a}}(\mathbf{b})}{\langle \mathbf{a},\mathbf{a}\rangle}$

and,

- $\dfrac{\partial}{\partial u_j}\left(\dfrac{\partial \mathbf{x}_m}{\partial \xi_1}\right) = \dfrac{\partial \mathbf{N}}{\partial \xi_1}\mathbf{M}\dfrac{\partial \mathbf{x}_m}{\partial u_j} = \dfrac{\partial \mathbf{N}}{\partial \xi_1}\mathbf{M}\dfrac{\partial \mathbf{u}}{\partial u_j} = \dfrac{\partial \mathbf{N}}{\partial \xi_1}\mathbf{M}\mathbf{z}_j$
- $\dfrac{\partial}{\partial u_j}\left(\dfrac{\partial \mathbf{x}_m}{\partial \xi_2}\right) = \dfrac{\partial \mathbf{N}}{\partial \xi_2}\mathbf{M}\dfrac{\partial \mathbf{x}_m}{\partial u_j} = \dfrac{\partial \mathbf{N}}{\partial \xi_2}\mathbf{M}\dfrac{\partial \mathbf{u}}{\partial u_j} = \dfrac{\partial \mathbf{N}}{\partial \xi_2}\mathbf{M}\mathbf{z}_j$
- $\dfrac{\partial \mathbf{G}}{\partial u_j} = \mathbf{N}\mathbf{L}\dfrac{\partial \mathbf{u}}{\partial u_j} = \mathbf{N}\mathbf{L}\mathbf{z}_j$

where $\mathbf{z}_j$ is a 3×1 column vector such that $\begin{cases} z_{j_i} = 0, & \text{if} \quad i \neq j \\ z_{j_i} = 1, & \text{if} \quad i = j \end{cases}$, while the rest of these variables have the same meaning as in section 2.1

B

Analytical Models

Moreira et al. (2020) used the expressions from the following sections to determine the total fracture toughness from the experimental data obtained from different tests. One could use the compliance of the specimens with initial crack length, to estimate the load displacement response in the elastic region. Further, by considering an array of crack lengths (a) with small increments, one could derive the load for crack growth from the strain energy release rate (SERR) expression and then estimate corresponding displacement using the compliance for that crack length, to derive the load displacement response in the fracture regime.

DCB & ADCB

DCB & ADCB are tension type fracture test with predominantly mode-I load. Load is applied in opposing directions on the two adherends similar to peeling as shown in fig. 2.10a. Following are the closed form expressions for the analytical model from Moreira et al. (2020) applicable for both specimen. The only difference is that in case of DCB, the properties of upper and lower adherends are the same.

Based on Timoshenko beam theory and the Castigliano theorem, one could express the compliance of the peel type DCB & ADCB specimens using

$$C = \frac{\delta}{P} = \left[\frac{a^3}{3}\left(\frac{1}{D_u} + \frac{1}{D_l}\right)\right] + \left[\frac{6a}{5BG_{13}}\left(\frac{1}{h_u} + \frac{1}{h_l}\right)\right] \tag{B.1}$$

where $D_u = E_{1u}I_u$, $D_l = E_{1l}I_l$, E_1 is the elastic modulus, $I = \frac{Bh^3}{12}$ is the second moment of area, while the rest of the variable carry the same notation as in section 2.2.

Using the compliance from eq. (B.1) and the Irwin-Kies equation (eq. (2.26)), the SERR for DCB & ADCB is

$$G_T = \frac{P^2}{2B}\left\{\left[a^2\left(\frac{1}{D_u} + \frac{1}{D_l}\right)\right] + \left[\frac{6}{5BG_{13}}\left(\frac{1}{h_u} + \frac{1}{h_l}\right)\right]\right\} \tag{B.2}$$

From eq. (B.1) and eq. (B.2), the crack length a for a given δ, is determined by solving the polynomial expression

$$F_1 a^6 + F_2 a^4 + F_3 a^2 + F_4 = 0 \tag{B.3}$$

where the equation constants are

$$F_1 = \frac{2G_T B}{9}\left(\frac{1}{D_u}+\frac{1}{D_l}\right)^2$$
$$F_2 = \frac{4G_T}{5G_{13}}\left(\frac{1}{D_u}+\frac{1}{D_l}\right)\left(\frac{1}{h_u}+\frac{1}{h_l}\right)$$
$$F_3 = \left[\frac{12G_T}{5G_{13}}\left(\frac{1}{h_u}+\frac{1}{h_l}\right)\right]^2 - \left[\delta^2\left(\frac{1}{D_u}+\frac{1}{D_l}\right)\right]$$
$$F_4 = \frac{-6\delta^2}{5BG_{13}}\left(\frac{1}{h_u}+\frac{1}{h_l}\right)$$

Although eq. (B.3) has 6 roots, only one of them is real and positive. Thereby giving a unique solution for the crack length a.

SLB & ASLB

SLB & ASLB are three point bending type fracture test with predominantly mode-II load. Load is applied at specimen half length on the upper adherend with pinned support as shown in fig. 2.10b. Following are the closed form expressions for the analytical model from Moreira et al. (2020) applicable for both specimen. The only difference is that in case of SLB, the properties of upper and lower adherends are the same.

Based on Timoshenko beam theory and the Castigliano theorem, one could express the compliance for SLB & ASLB specimens using

$$C = \frac{\delta}{P} = \frac{1}{12}\left[a^3\left(\frac{1}{D_u}-\frac{1}{D_m}\right)+\frac{2L^3}{D_m}\right]+\frac{3a}{10Bh_uG_{13}}+\frac{BC_1\,(2L-a)}{16{D_m}^2} \tag{B.4}$$

where D_u has the same definition as in the case of DCB & ADCB,

$$D_m = E_1 B\left(\frac{{h_u}^3+{h_l}^3}{12}+h_u{d_u}^2+h_l{d_l}^2\right)$$
$$d_u = \frac{h_l(h_u+h_l)}{2(h_u+h_l)}$$
$$d_l = \frac{h_u+h_l}{2}-d_u$$
$$C_1 = \frac{{E_1}^2}{G_{13}}\left\{h_l\left(d_l+\frac{h_l}{2}\right)^4-\frac{7}{15}\left(d_l+\frac{h_l}{2}\right)^5\right.$$
$$+\left(-d_l+\frac{h_l}{2}\right)^3\left[\frac{1}{5}\left(-d_l+\frac{h_l}{2}\right)^2-\frac{2}{3}\left(d_l+\frac{h_l}{2}\right)^2\right]$$
$$+\frac{8}{15}\left[\left(d_u+\frac{h_u}{2}\right)^5-\left(-d_l+\frac{h_l}{2}\right)^5\right]$$
$$\left.-\frac{8}{3}h_ld_l\left(-d_l+\frac{h_l}{2}\right)^3-4{h_l}^2{d_l}^2\left(-d_l+\frac{h_l}{2}\right)\right\}$$

while the rest of the variable carry the same notation as in section 2.2.

Using the compliance from eq. (B.4) and the Irwin-Kies equation (eq. (2.26)), the SERR for SLB & ASLB is

$$G_T = \frac{P^2}{2B}\left\{\left[\frac{a^2}{4}\left(\frac{1}{D_u}+\frac{1}{D_m}\right)\right]+\frac{3}{10Bh_uG_{13}}+\frac{BC_1}{16{D_m}^2}\right\} \tag{B.5}$$

From eq. (B.4) and eq. (B.5), the crack length a for a given δ, is determined by solving the polynomial expression

$$F_1a^6+F_2a^4+F_3a^3+F_4a^2+F_5a+F_6=0 \tag{B.6}$$

where the equation constants are

$$\begin{aligned}
P_1 &= \left(\frac{1}{D_u}-\frac{1}{D_m}\right)\\
P_2 &= \left(\frac{1}{D_u}+\frac{1}{D_m}\right)\\
P_3 &= \frac{3}{10Bh_uG_{13}}-\frac{BC_1}{16{D_m}^2}\\
P_4 &= \frac{3}{10Bh_uG_{13}}+\frac{BC_1}{16{D_m}^2}\\
P_5 &= \frac{L^3}{6D_m}+\frac{LBC_1}{8{D_m}^2}\\
F_1 &= 2BG_T\left(\frac{P_1}{12}\right)^2\\
F_2 &= \frac{1}{3}BG_TP_1P_3\\
F_3 &= \frac{1}{3}BG_TP_1P_5\\
F_4 &= 2BG_TP_3^2-\delta^2\frac{P_2}{4}\\
F_5 &= 4BG_TP_3P_5\\
F_6 &= 2BG_TP_5^2-\delta^2P_4
\end{aligned}$$

Although eq. (B.3) has 6 roots, only one of them is real and positive. Thereby giving a unique solution for the crack length a.

ENF

ENF is a three point bending type fracture test with mode-II load. Load is applied at specimen half length on the upper adherend with pinned support as shown in fig. 2.10c. Following are the closed form expressions for the analytical model from Moreira et al. (2020) applicable for ENF specimen.

Using the same method as above, compliance for ENF specimen is

$$C = \frac{\delta}{P} = \frac{3a^3 + 2L^3}{8E_1Bh^3} + \frac{3L}{10G_{13}Bh} \tag{B.7}$$

where the variable carry the same notation as in section 2.2.

Using the compliance from eq. (B.7) and the Irwin-Kies equation (eq. (2.26)), the SERR for ENF specimen is

$$G_T = \frac{9P^2a^2}{16B^2h^3E_1} \tag{B.8}$$

$$G_T \left\{ P_1a^3 + P_2 \right\}^2 = \frac{9\delta^2}{P_3}a^2 \tag{B.9}$$

From eq. (B.7) and eq. (B.8), the crack length a for a given δ, is determined by solving the polynomial expression

$$F_1a^6 + F_2a^3 + F_3a^2 + F_4 = 0 \tag{B.10}$$

where the equation constants are

$$\begin{aligned}
P_1 &= \frac{3}{8E_1Bh^3} \\
P_2 &= \frac{2L^3}{8E_1Bh^3} + \frac{3L}{10G_{13}Bh} \\
P_3 &= 16B^2h^3E_1 \\
F_1 &= G_TP_1^2 \\
F_2 &= 2G_TP_1P_2 \\
F_3 &= \frac{9\delta^2}{P_3} \\
F_4 &= G_TP_2^2
\end{aligned}$$

Although eq. (B.3) has 6 roots, only one of them is real and positive. Thereby giving a unique solution for the crack length a.

C Scripts & simulation data

The tests from chapter 3 were conducted using the *czmtestkit* package developed to test user element subroutines of cohesive zone models for implementation with Abaqus/CAE and to implement the mode partitioning method from section 3.1.1 to characterize the mixed-mode response of interfaces. Table C.1 provides links to the scripts used in running the tests from chapter 3. The documentation presented in table C.1 includes examples for implementing the mode partitioning method and comparing the small displacement and the large displacement formulations.

Package:	
Source code	doi:10.4121/19410146
Documentation	`http://czmtestkit.readthedocs.io/`
Data:	
section 4.2 - BK criteria	doi:10.4121/19410773
section 4.2 - power law	doi:10.4121/19411130
section 5.1	doi:10.4121/19411343
section 5.2	doi:10.4121/19411157
section 5.3	doi:10.4121/19410401

Table C.1: Links to software and simulation data